STRUCTURAL SCIENCE
CRYSTAL ENGINEERING
MATERIALS

ISSN 2052-5206

Phase transitions and (*p*–*T*–*X*) behaviour of centrosymmetric perovskites: modelling with transformed crystallographic data

Noel W. Thomas*

Werkstofftechnik Glas and Keramik, Hochschule Koblenz, Rheinstrasse 56, 56203 Hoehr-Grenzhausen, Germany.
*Correspondence e-mail: thomas@hs-koblenz.de

Received 5 August 2021
Accepted 30 November 2021

Edited by R. Černý, University of Geneva, Switzerland

Dedicated to the memory of Christopher Jason Thomas (30.12.1988–21.10.2021).

Keywords: perovskite; centrosymmetric; phase transition; *p*–*T*–*X*; octahedral distortion; octahedral tilting; structural modelling.

Supporting information: this article has supporting information at journals.iucr.org/b

A reversible transformation of the unit-cell parameters and atomic coordinates of centrosymmetric perovskites ABX_3 into a Cartesian space is defined. Analytical expressions for the three vectors for the pseudocubic cell and three vectors for a BX_6 octahedron are derived for space groups *Pbmn*, *Cmcm*, *Ibmm*, *P*4/*mbm*, *P*4/*nmc*, *I*4/*mcm* and $R\bar{3}c$. The following structural parameters may be derived from these vectors: up to six pseudocubic parameters defining octahedral geometry; length- and angle-based octahedral distortion parameters λ and σ; inclination angles of tilted octahedra, θ_1, θ_2 and θ_3; angles of tilt of octahedra; AX_{12}:BX_6 polyhedral volume ratio, V_A/V_B; parameters η_A and η_B defining the relative contraction of inner AX_8 polyhedra and expansion of BX_6 octahedra due to octahedral tilting. The application of these parameters is demonstrated by reference to published crystal structures. The variation of η_A and η_B with temperature in the compositional series $Sr_xBa_{1-x}SnO_3$ and $Sr_xBa_{1-x}HfO_3$, as well as the temperature series of $BaPbO_3$ and $CaTiO_3$, is related to the sequence of phases *Pbmn* → *Ibmm*→ $Pm\bar{3}m$. Stabilization of the *Cmcm* phase is likewise interpreted in terms of these two parameters for $NaTaO_3$ and $NaNbO_3$. The pressure evolution of the structures of $MgSiO_3$, $YAlO_3$, $(La_{1-x}Nd_x)GaO_3$ ($0 \leq x \leq 1$) and $YAl_{0.25}Cr_{0.75}O_3$ is modelled with the appropriate structural parameters, thereby also addressing the characteristics of the *Pbmn* → $R\bar{3}c$ transition. Simulation of $MgSiO_3$ up to 125 GPa and of $YAlO_3$ up to 52 GPa in space group *Pbnm* is carried out by using the Birch–Murnaghan equation of state. In both cases, full sets of oxygen coordinates assuming regular octahedra are generated. Octahedral distortion is also modelled in the latter system and predicted to have a key influence on structural evolution and the sequence of phase transitions. The core modelling procedures are made available as a Microsoft *Excel* file.

1. Introduction: the modelling of octahedral tilting in perovskites

Synthetic perovskite-related compounds continue to attract the attention of many scientists and technologists, irrespective of whether they are working, for example, on the development of lead-free piezoelectric ceramics (Shrout & Zhang, 2007) or on organolead halide ABX_3 nanocrystals for photochemical cells (Jena *et al.*, 2019). In general, the current availability of high-quality structural data evokes the need for all the nuances of structural change under varying conditions of pressure, temperature and composition] (*p*–*T*–*X*) to be precisely modelled. This expectation is particularly poignant in the case of perovskite-related compounds, ABX_3, since, according to Mitchell (2002*a*), all elements, apart from the noble gases, can be found in a variant of these. In the pioneering work of Megaw (1973), their structures were regarded as comprising three essential features: (*a*) tilting of

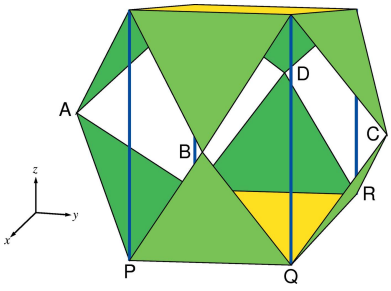

the anion octahedra; (*b*) displacements of the cations; (*c*) octahedral distortions. Definitive work by Glazer (1972) led to a system of classification based on the sense of tilt of the three tetrad axes of corner-linked regular octahedra about three perpendicular, or nearly perpendicular crystal axes.

A regular octahedron is characterized by three pairs of opposite vertices that are linked by stalks of equal length passing through its mid-point at right angles to one another. Two lines of regular octahedra are shown in Figs. 1(*a*) and 1(*b*), as they arise in space group *Pbnm*.

Zigzag chains of adjacent octahedral stalks of uniform length *s* are formed, these lying in planes PQRS and TUVW. When viewed along the y_{PC} axis-of-tilting, the red and blue octahedra are seen to be rotated in opposite senses [Fig. 1(*c*)], leading to Glazer notation b^-. By comparison, the red and green octahedra are rotated in the same sense [Fig. 1(*d*)]. This leads to the notation c^+, since the tilt angle is different. As tilting around the x_{PC} and y_{PC} axes is equivalent, the three-dimensional tilt system in *Pbnm* is denoted by $a^-a^-c^+$ (Glazer, 1972).

In this now well established $a^\#b^\#c^\#$ nomenclature, superscripts # can be +, − or 0, denoting the angles of tilt of neighbouring octahedra along the three pseudocubic axes as in-phase (+), anti-phase (−) or zero. Importantly, Glazer (1972) also showed that the 23 tilt systems for regular octahedra correlated with 15 alternative space groups. As well as aiding the correct interpretation of perovskite diffraction patterns (Glazer, 1975), these correlations stimulated group-theoretical analysis of perovskites, their being confirmed significantly later by Howard & Stokes (1998, 2002). The latter

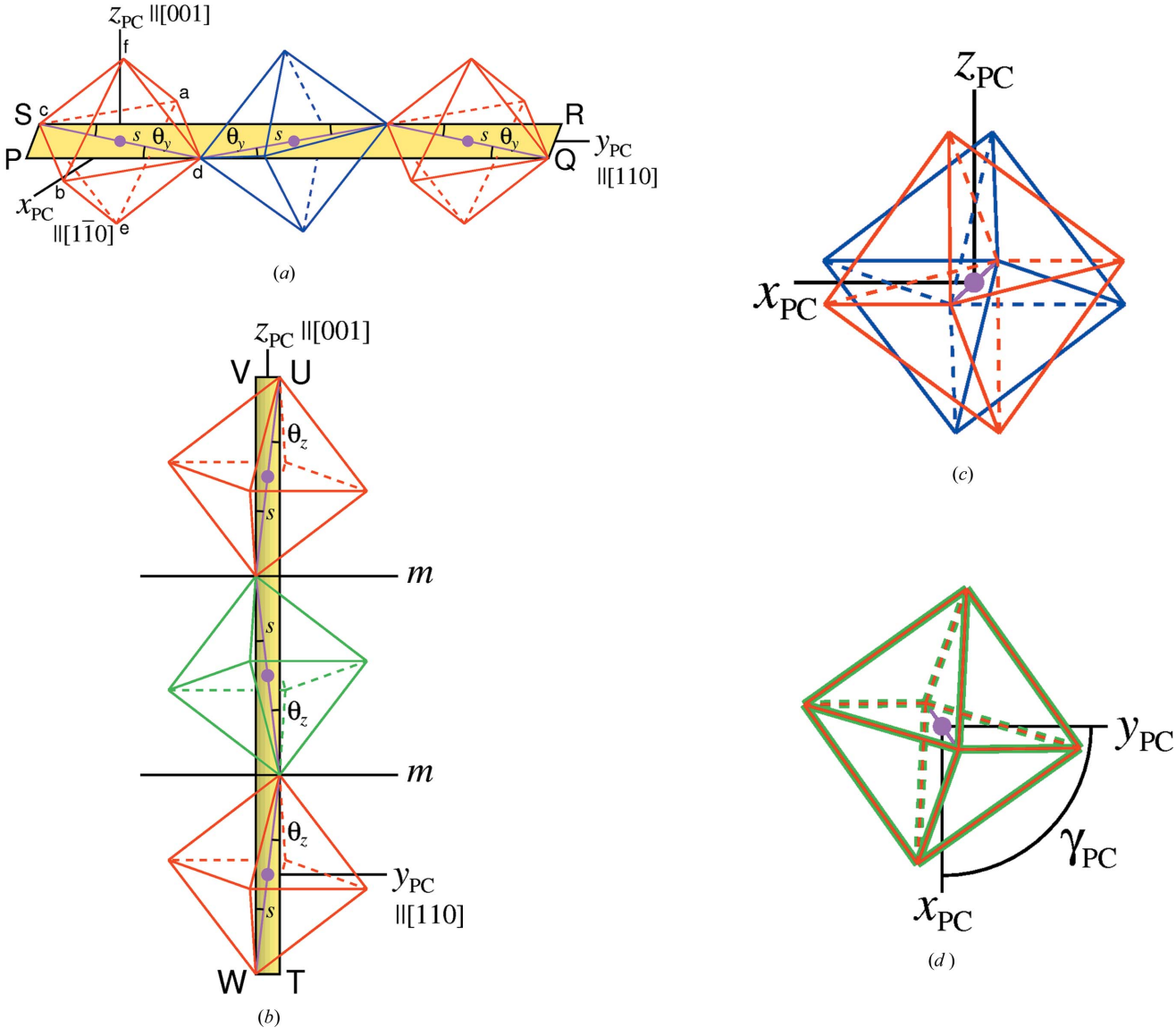

Figure 1
Tilting of regular octahedra about the x_{PC} and y_{PC} axes, as in space group *Pbnm*. Pseudocubic axes x_{PC}, y_{PC} and z_{PC} are directed parallel to orthorhombic vectors $[1\bar{1}0]$, [110] and [001], respectively. (*a*) Tilting around the y_{PC} axis (in clinographic projection) with θ_y the angles of inclination of stalks of length *s* to the axis; (*b*) Tilting around the z_{PC} axis (head-on view showing mirror planes); (*c*) y_{PC}-axis tilting [as in (*a*)] viewed along the y_{PC} axis towards the origin; (*d*) z_{PC}-axis tilting [as in (*b*)] viewed along the z_{PC} axis towards the origin.

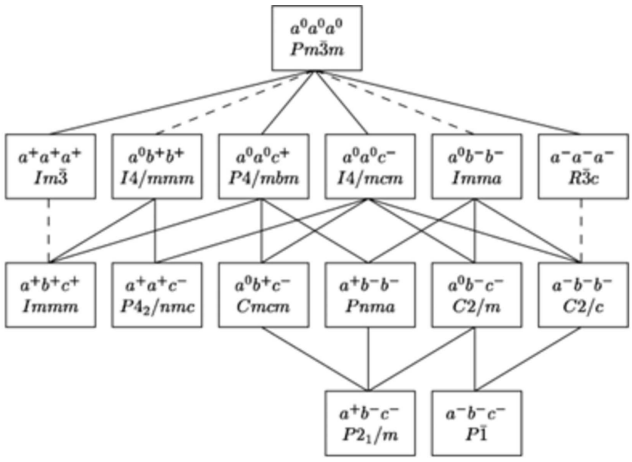

Figure 2
Group–subgroup relationships among the 15 perovskite space groups arising from the tilting of regular octahedra. A dashed line signifies that the corresponding phase transition must be first order (Howard & Stokes, 2002). Reproduced with permission of the International Union of Crystallography.

work led to minor modifications to the space groups originally assigned by Glazer and established a top-down, hierarchical system of group–subgroup relationships starting from the cubic $Pm\bar{3}m$ aristotype for perovskite structures with tilted, regular octahedra (Fig. 2).

Two independent contributions concerning octahedral tilting in perovskites were made by Woodward (1997*a*,*b*) and Thomas (1996). Woodward (1997*a*) concluded that perfectly regular octahedra could not be linked together in some tilt systems. The contentious space groups were subsequently narrowed down to *Cmcm* (tilt system $a^0b^+c^-$) and $P4_2/nmc$ ($a^+a^+c^-$) by Howard & Stokes (1998), with only the latter requiring irregular octahedra. The work of Thomas (1996), by comparison, was primarily concerned with the dependence of AX_{12}:BX_6 polyhedral volume ratio, V_A/V_B, on octahedral tilting in orthorhombic and tetragonal perovskites. Inclination angles θ_y and θ_z in Figs. 1(*a*) and 1(*b*), and by extension θ_x, were used to relate octahedral stalk lengths *s* and tilting to the lengths of pseudocubic cell axes 1, 2 and 3 and therefore cell volume [equation (1)].

$$V_A/V_B \approx 6\cos^2\left[(\theta_1+\theta_2)/2\right]\cos\theta_3 - 1 \qquad (1)$$

This form results from the coupling of inclination angles θ_1 and θ_2 when pseudocubic axes 1 and 2 are oriented at approximately 45° to the crystal axes. In untilted structures (with $\theta_1 = \theta_2 = \theta_3 = 0$), V_A/V_B is exactly equal to five (Thomas, 1989).

Tamazyan & van Smaalen (2007) subsequently argued that inclination angles θ_1, θ_2 and θ_3 defined by Thomas (1996) were unnecessarily influenced by octahedral distortion. They therefore proposed an alternative method of calculating tilt angles, although this was at the expense of losing the simple link to polyhedral volume ratio expressed by equation (1). Later work by Wang & Angel (2011) restored the link between octahedral tilting and ratio V_A/V_B, employing a group-theoretical, rather than a geometrical approach to separate octahedral tilting and distortion. These authors expressed the ratio V_A/V_B as a function of the amplitudes of the normal modes in a cubic perovskite, rather than by direct calculation from anion coordinates in experimentally determined crystal structures.

The conflict between geometrical, *i.e.* crystal-chemical and group-theoretical methods in describing perovskite structures is somewhat contrived, since both have legitimate fields of application and ultimately have similar aims. This was made clear in seminal work by Knight (2009), who utilized group-theoretical methods to develop a general parameterization of centrosymmetric perovskites based on symmetry-adapted basis vectors of the $Pm\bar{3}m$ phase. He also pointed to difficulties with a method earlier proposed by this author for a general crystal-chemical parameterization of centrosymmetric perovskites (Thomas, 1998). Two specific problems were identified, (*a*) that the method was 'geometrically complex'; and (*b*) that it relied 'totally on an empirical analysis of known crystal structures'. He also made the important point, (*c*), that the *A* site has a coordination number less than 12 due to a geometrically complex coordination polyhedron (Knight, 2009). In the current work, point (*a*) is addressed by focusing on the distortion of centrosymmetric octahedra as independent geometrical forms. Point (*b*) is addressed by deriving analytical expressions dependent on space group for the three stalk vectors defining octahedral geometry. Point (*c*) is addressed by developing a simple parameterization based on AX_8 sub-polyhedra that correlates with the tilt classification system of Glazer (1972). Details of these methodological improvements are given in the following section.

2. Elements of the revised crystal-chemical method

2.1. Pseudocubic representations of octahedra

In order that an object can be described as an octahedron, it requires three recognisable pairs of opposite vertices that may be linked to each another by vectors. If the ends of the stalks of a regular octahedron [Fig. 3(*a*)] are randomly displaced by limited amounts [Fig. 3(*b*)], the resulting form is still recognisable as an octahedron [Fig. 3(*c*)]. The six independent vertices lead to six sets of $[x, y, z]$ triplets in Cartesian space, *i.e.* 18 parameters. If only the form of the octahedron is relevant, and not its absolute position or orientation, these 18 parameters are reduced to 12 by subtracting six parameters: three to fix one vertex in space at [0,0,0] and three to define the orientation of the octahedron. In Fig. 3(*c*), one vertex has been fixed at [0,0,0] and the octahedron so rotated that the opposite vertex is fixed at $[0\,,0, z_1]$. A further rotation of the octahedron about the *z* axis has been carried out to fix a vertex at $[0, y_2, z_2]$. The total of six coordinate-components equal to zero here signifies a reduction in independent parameters from 18 to 12, *i.e.* (z_1; y_2z_2; $x_ny_nz_n$; n = 3,5). If, however, the translations at opposite ends of the three stalks are equal and opposite [Fig. 3(*d*)], a centrosymmetric octahedron results [Fig. 3(*e*)], in which the three stalks bisect one other at the centre of symmetry. Only one end of a stalk needs to be fixed

in space in order to define the position of the opposite end, so that the number of independent parameters is halved to six [Fig. 3(*e*)]: (z_1; y_2z_2; $x_3y_3z_3$). This situation applies to all perovskites with *B* ions located at centres of symmetry.

The six independent parameters of a centrosymmetric octahedron may be assigned to three stalk lengths a_1, a_2, a_3 and three angles of intersection of the stalks, θ_{12}, θ_{23} and θ_{31}. In order to visualize the extent of its distortion, a parallelepiped enclosing the octahedron may be constructed by displacing the three stalk vectors to a common origin (Fig. 4).

As the three independent edge lengths of the parallelipiped are approximately equal, it may also be termed a pseudocube. Such a pseudocube is defined by the same six parameters as the octahedron, *i.e.* a_1, a_2, a_3, θ_{12}, θ_{23} and θ_{31}. It follows that regular octahedra would lead to pseudocubic representations of octahedra (PCRO) of cubic form.

In the case of the non-centrosymmetric octahedron of Fig. 3(*c*), the six octahedral vertices do not touch their parallelogram faces at the meeting points of the four quadrants [Fig. 4(*d*)]. The 12 independent parameters may be accommodated by noting the 2D polar coordinates [r, ϕ] of the three emergent octahedral vertices, giving rise to additional parameters r_1, r_2, r_3, ϕ_1, ϕ_2 and ϕ_3. Thus the PCRO construction is of general validity for visualizing distorted octahedra. Its parameterization may prove to be useful for characterizing non-centrosymmetric and polar perovskites in future work. The transformation between octahedron and PCRO is also reversible.

An advantage of the PCRO visualization method is that the aggregate distortion parameters representing normal and shear distortion developed for pseudocubic representations of tetrahedra (PCRT), λ and σ, (Reifenberg & Thomas, 2018; Fricke & Thomas, 2021) may be taken over without modification [equations (2), (3)].

$$\lambda = \frac{|a_1 - L_0| + |a_2 - L_0| + |a_3 - L_0|}{3L_0} \quad \text{with} \quad L_0 = \frac{(a_1 + a_2 + a_3)}{3} \tag{2}$$

$$\sigma(^\circ) = \frac{\left|\theta_{12}(^\circ) - 90^\circ\right| + \left|\theta_{23}(^\circ) - 90^\circ\right| + \left|\theta_{31}(^\circ) - 90^\circ\right|}{3} \tag{3}$$

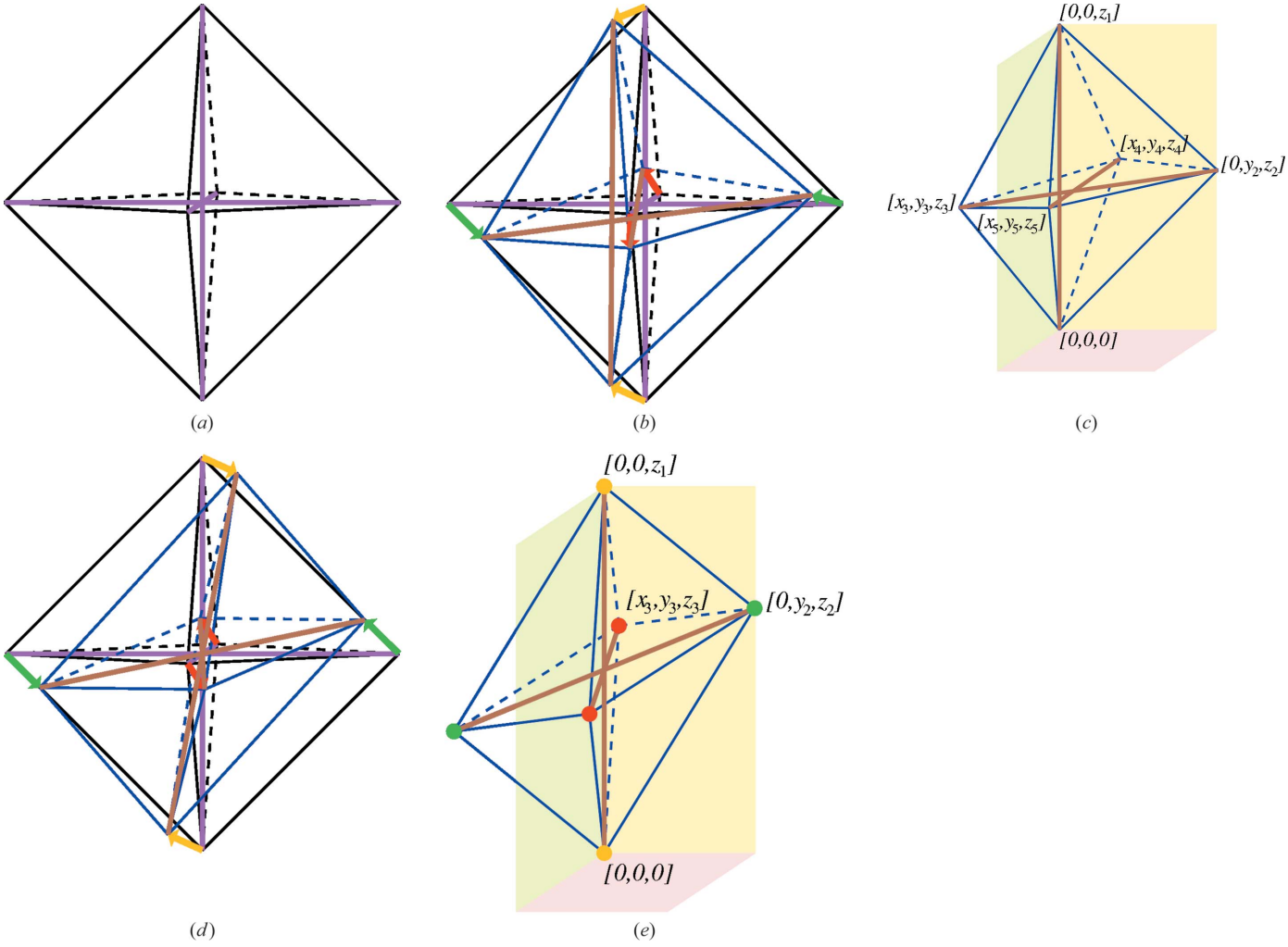

Figure 3
The number of independent parameters of a generalized, isolated centrosymmetric octahedron is equal to six. Views (*a*) to (*e*) discussed in §2.1.

In this connection, the following values are obtained for the centrosymmetric and non-centrosymmetric octahedra of Figs. 3(*e*) and 3(*c*), respectively: [λ,σ] = [0.0367, 11.90°]; [λ,σ] = [0.0370, 7.10°]. It follows that the centrosymmetric octahedron displays a higher degree of angular distortion here. Furthermore, if the angular distortion parameters are expressed in radians instead of degrees, the relative degree of shear versus normal distortion can be quantified. Since 11.90° correspond to 0.21 and 7.10° to 0.12 radian, it follows that the shear distortion is greater than the normal distortion in both cases.

2.2. Parameterization of PCRO in terms of three vectors

The octahedra in perovskites are not isolated but form a three-dimensional corner-sharing network. Their crystal structural parameters, *i.e.* space group, unit-cell parameters and atomic coordinates, deliver full information on octahedral distortion, tilting and connectivity. Importantly, space group symmetry ensures connectivity. Once the distortion and tilting of a single octahedron in a structure with only one symmetry-independent octahedron has been defined, the distortions and tilting of all the other octahedra in the unit cell follow. To convey full information on the tilting of this single octahedron in a structure, its PCRO may be described by the three Cartesian stalk vectors, $\mathbf{a}_1$, $\mathbf{a}_2$ and $\mathbf{a}_3$ along its pseudocube edges. Generalized, analytical expressions for these vectors in different space groups may be derived inductively from known crystal structures. This process is described in §2.2.1 for space group *Pbnm* with *B* ions located at 4*b* special positions. The three vectors defining the axes of the pseudocubic unit cell are likewise defined in this Cartesian space, so that inclination angles of the stalks to the three pseudocubic axes, θ_1, θ_2 and θ_3 may straightforwardly be calculated [see Fig. 1, equation (1) and §2.3]. In addition, the method also allows calculation of tilt angles ϕ_a, ϕ_b and ϕ_c of the octahedra around the three pseudocubic axes, even when the octahedra are distorted.

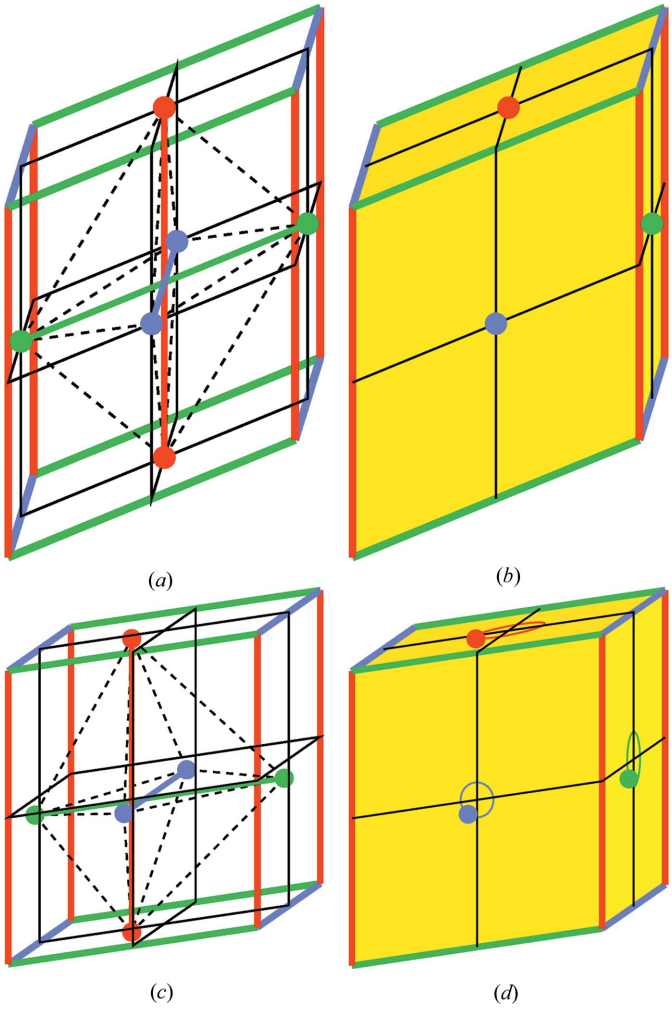

Figure 4
Visualization of the distortion of octahedra by enclosure in a pseudocube: (*a*), (*b*): centrosymmetric; (*c*), (*d*) non-centrosymmetric.

2.2.1. Space group *Pbnm* with *B* ions at 4*b* positions. The octahedral cage coordinating the *B* ion at $0\frac{1}{2}0$ in the unit cell of orthorhombic space group *Pbnm* may be taken, this being the **cab** setting of space group 62 with standard symbol *Pnma*. $0\frac{1}{2}0$ is one of the 4*b* special positions, with *X*1 ions in 4*c* special positions and *X*2 ions in 8*d* general positions (see Table S1 in the supporting information).[1]

Derivation of the analytical form of stalk, or equivalently PCRO vectors $\mathbf{a}_1$, $\mathbf{a}_2$ and $\mathbf{a}_3$ starts by taking an example structure, such as $CaTiO_3$ at 296 K [Yashima & Ali (2009); ICSD code 162908]: a = 5.3709 Å, b = 5.4280 Å, c = 7.6268 Å; x(O1) = 0.0708, y(O1) = 0.4830, x(O2) = 0.7113, y(O2) = 0.2891, z(O2) = 0.0375; z(O1) has the fixed value of $\frac{1}{4}$.

The essential step is to convert from numerical fractional coordinates of the titanium ion and its six oxygen neighbours (Table 1, columns 2–4) to analytical fractional coordinates (Table 1, columns 8–10). One way to generate the numerical fractional coordinates would be to use a simple computer program to generate the Cartesian coordinates of the titanium and oxygen ions. (Table 1, columns 5–7). The numerical fractional coordinates (Table 1, columns 2–4) would then follow by multiplying these by the inverse orthogonalization matrix, in this trivial case

$$\begin{pmatrix} 1/a & 0 & 0 \\ 0 & 1/b & 0 \\ 0 & 0 & 1/c \end{pmatrix}.$$

Letters a to f of the oxygen ions correspond to the atom labels in Fig. 1(*a*). They are based on the principle that the octahedral stalk from a to b is oriented closest to the x_{PC} axis in the positive direction, with the stalks from c to d and from e to f oriented closest to the positive y_{PC} and z_{PC} directions, respectively.

The analytical expressions in columns 8 to 10 of Table 1 are obtained by inspection: the values in columns 2 to 4 are compared with the starting values of x(O1), y(O1), x(O2), y(O2) and z(O2). It is important to note that the results depend on the convention used for expressing these para-

[1] Since oxides are exclusively considered in this work, the notation 'O1,O2 . . . ' is used interchangeably with '*X*1,*X*2 . . . '.

Table 1
Calculation of analytical fractional coordinates of the six oxygen anions coordinating the titanium ion in $CaTiO_3$ located at $0,\frac{1}{2},0$.

Atom	Numerical fractional coordinates			Cartesian coordinates			Analytical fractional coordinates		
	x	y	z	x_C	y_C	z_C	x	y	z
Ti (4*b*)	0	0.5	0	0.0000	2.7140	0.0000	0	$\frac{1}{2}$	0
O a (8*f*)	−0.2113	0.7891	0.0375	−1.1349	4.2832	0.2860	$-x(O2)+\frac{1}{2}$	$y(O2)+\frac{1}{2}$	$z(O2)$
O b (8*f*)	0.2113	0.2109	−0.0375	1.1349	1.1448	−0.2860	$x(O2)-\frac{1}{2}$	$-y(O2)+\frac{1}{2}$	$-z(O2)$
O c (8*f*)	−0.2887	0.2891	0.0375	−1.5506	1.5692	0.2860	$x(O2)-1$	$y(O2)$	$z(O2)$
O d (8*f*)	0.2887	0.7109	−0.0375	1.5506	3.8588	−0.2860	$-x(O2)+1$	$-y(O2)+1$	$-z(O2)$
O e (4*c*)	−0.0708	0.5170	−0.25	−0.3803	2.8063	−1.9067	$-x(O1)$	$-y(O1)+1$	$-\frac{1}{4}$
O f (4*c*)	0.0708	0.4830	0.25	0.3803	2.6217	1.9067	$x(O1)$	$y(O1)$	$\frac{1}{4}$

Table 2
The three vectors defining the PCRO with mid-point $0,\frac{1}{2},0$ in space group *Pbnm*.

Stalk	PCRO vector	Cartesian components			Nearest pseudocubic axes	
		X	Y	Z	Pseudocubic	Orthorhombic
O b ← O a	$\mathbf{a}_1$	$a(2x(O2)-1)$	$-2by(O2)$	$-2cz(O2)$	x_{PC}	$]0\bar{1}0]$
O d ← O c	$\mathbf{a}_2$	$-2a(x(O2)-1)$	$-b(2y(O2)-1)$	$-2cz(O2)$	y_{PC}	[110]
O f ← O e	$\mathbf{a}_3$	$2ax(O1)$	$b(2y(O1)-1)$	$c/2$	z_{PC}	[001]

meters. For example, the alternative of $x(O1) = 0.4292$ and $y(O1) = -0.0170$, although symmetrically equivalent, would lead instead to the results $x(O\ e) = x(O1) - \frac{1}{2}$ and $y(O\ e) = -y(O1) + \frac{1}{2}$.

The three vectors for the PCRO are now formed in Table 2 by taking the differences in the analytical fractional coordinates for atom pairs (a,b), (c,d) and (e,f) given in Table 1. Cartesian vectors are formed by multiplying these differences by the orthogonalization matrix

$$\begin{pmatrix} a & 0 & 0 \\ 0 & b & 0 \\ 0 & 0 & c \end{pmatrix}.$$

The Cartesian axes are parallel to the axes of the orthorhombic unit cell in this case.

By adopting this analytical representation, vectors $\mathbf{a}_1$, $\mathbf{a}_2$ and $\mathbf{a}_3$ are no longer tied to the example structure of $CaTiO_3$: they apply to all perovskites in space group *Pbnm*, provided that the *B* ions occupy 4*b* sites and that the correct convention in choosing the values parameters $x(O1)$, $y(O1)$, $x(O2)$, $y(O2)$ and $z(O2)$ has been followed. All eight crystallographic parameters are involved in defining the geometry of the PCRO in space group *Pbnm*: a, b, c, $x(O1)$, $y(O1)$, $x(O2)$, $y(O2)$, $z(O2)$. For regular octahedra, six of these eight degrees of freedom (d.o.f.) would be used up in forming octahedra of a particular volume, with five defining the regular form and the sixth the volume. The remaining two d.o.f. would be used to define the unit-cell parameters and octahedral tilting. If the octahedra were only approximately regular, as is generally the case, more d.o.f. would be available for optimizing the octahedral tilting and unit-cell volume, in response to different *A* and *B* ion radii or to changing temperature or hydrostatic pressure. Thus the idea of structural compromise in forming connected octahedral networks in perovskites can be modelled in response to varying (p–T–X) conditions.

2.2.2. Other space groups. The other space groups analysed in this work are those that commonly arise in experimentally determined crystal structures. They span the following space groups: *Pbmn* (*B* ions in 4*a* sites), *Cmcm*, *Ibmm*, *P*4/*mbm*, $P4_2/nmc$, *I*4/*mcm*, $R\bar{3}c$, $Pm\bar{3}m$. Tables similar to Table 2 are generated for them in §S2 of the supporting information.

2.3. Implementation of the crystallographic to structural transformation in the Microsoft *Excel* Solver environment

Structural *analysis* requires a one-way transformation from crystallographic to structural parameters. For example, crystallographic parameters a, b, c, x_i, y_i, z_i are transformed to structural parameters such as PCRO parameters and tilt angles. By comparison, structural prediction requires a reversible transformation between the two parameter sets. The modeller will seek to establish systematic variations in the structural parameters with (p–T–X). If successful, interpolations and extrapolations to other (p–T–X) values can be made before reverse-transforming to crystallographic parameters. This technique has been demonstrated for olivines (Thomas,

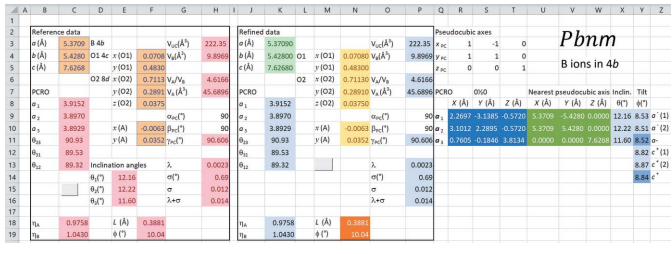

Figure 5
Screenshot of the *Pbnm* worksheet, which contains the reference data for $CaTiO_3$ at 296 K (Yashima & Ali, 2009). No refinement has taken place, since the entries in the 'Refined data' and 'Reference data' boxes are identical.

2017), coesite (Reifenberg & Thomas, 2018) and quartz (Fricke & Thomas, 2021).

The requirements of ease and flexibility of use together with a reversible transformation suggest that the Microsoft *Excel* Solver environment is appropriate for applying the method. In this connection, an *Excel* datafile already programmed is provided in the supporting information. This consists of eight worksheets for the different space groups. A screenshot of the worksheet for *Pbnm* with *B* ions in 4*b* positions is given in Fig. 5.

The user enters the crystallographic data in the 'Refined data' box in blocks K3:K5 (light-green background), N4:N8 and N10:N11 (mustard background), whereupon all the structural parameters are automatically calculated by *Excel*. The computational core of the spreadsheet is in blocks R9:T11 (deep-blue background) and U9:W11 (dark-green background). The formulas in these cells correspond to the entries in Table 2 and the pseudocubic axes in Cartesian coordinates, respectively. Values of all the structural parameters relating to octahedral distortion and tilting (light-blue background) can be seen as ways of describing the numerical values in these two blocks in a structurally meaningful way.

The purpose of the 'Reference data' box is threefold. First, it acts as a repository for the source, reference data (cells with orange background). Secondly, the dependent structural parameters can be calculated for this reference data by clicking on the button in cell C15.[2] Thirdly, both reference data and dependent structural parameters can be used as constraints in structural refinements, which apply to the cells in the 'Refined data' box.

The different types of structural parameters, all with light-blue background, are summarized as follows.

a) **PCRO parameters** a_1, a_2, a_3, θ_{23}, θ_{31}, θ_{12} are calculated as the lengths and intersectional angles of the vectors $\boldsymbol{a}_1$, $\boldsymbol{a}_2$, $\boldsymbol{a}_3$ in block R9:T11. For example, $\theta_{23} = \arccos(\mathbf{a}_2 \cdot \mathbf{a}_3/a_2a_3)$. **Aggregate distortion parameters** λ and σ [equations (2) and (3)] are calculated in block P13:P16, the latter quoted in both degrees and radians.

b) **Pseudocubic angle** $\gamma_{\rm PC}$ is calculated as the angle between pseudocubic axes $a_{\rm PC}$ and $b_{\rm PC}$ in cell P11: $\gamma_{\rm PC} = \arccos(\mathbf{a}_{\rm PC} \cdot \mathbf{b}_{\rm PC}/a_{\rm PC}b_{\rm PC})$.

c) **Inclination angles** θ_1, θ_2, θ_3 of the octahedral stalks are quoted in block X9:X11. These describe the relationship of the two sets of vectors in blocks R9:T11 and U9:W11 to one another. With respect to vector $\mathbf{a}_1$ in block R9:T9 and its nearest pseudocubic axis vector $\mathbf{a}_{\rm PC}$ in block U9:W9, the following applies:

$$\mathbf{a}_1 = \begin{pmatrix} a_{1X} \\ a_{1Y} \\ a_{1Z} \end{pmatrix};$$

$$\mathbf{a}_{\rm PC} = \begin{pmatrix} a_{{\rm PC},X} \\ a_{{\rm PC},Y} \\ a_{{\rm PC},Z} \end{pmatrix}.$$

The subscripts X, Y, Z here denote the Cartesian X, Y and Z components, respectively. It follows that

$$\begin{aligned}\theta_1 &= \arccos(\mathbf{a}_1 \cdot \mathbf{a}_{\rm PC}/a_1a_{\rm PC}) \\ &= \arccos\left(\left[a_{1X}a_{{\rm PC},X} + a_{1Y}a_{{\rm PC},Y} + a_{1Z}a_{{\rm PC},Z}\right]/a_1a_{\rm PC}\right) \quad (4)\end{aligned}$$

Substitution of

$$a_{\rm PC} = \begin{pmatrix} 2.2697 \\ -3.1385 \\ -0.5720 \end{pmatrix}$$

and

$$a_{\rm PC} = \begin{pmatrix} 5.3709 \\ -5.4280 \\ 0.0000 \end{pmatrix}$$

leads to θ_1 = 12.16°. Angles θ_2 and θ_3 are derived from the corresponding pairs ($\mathbf{a}_2$,$\mathbf{b}_{\rm PC}$) as well as ($\mathbf{a}_3$,$\mathbf{c}_{\rm PC}$), respectively.

d) The method of calculation of angles of tilt $\phi_{\rm a}$ and $\phi_{\rm c}$ in the $a^-a^-c^+$ tilt system of space group *Pbnm* is shown in Fig. 6. These angles constitute an alternative to the inclination angles for relating the two sets of vectors in blocks R9:T11 and U9:W11 to each other. Since tilt angles are to be calculated for distorted octahedra, the method evaluates the projections of oxygen atoms O a, O b, O c and O d in the planes perpendicular to pseudocubic axes $\mathbf{a}_{\rm PC}$, $\mathbf{b}_{\rm PC}$ and $\mathbf{c}_{\rm PC}$. These four atoms also define PCRO vectors $\mathbf{a}_1$ and $\mathbf{a}_2$: vector $\mathbf{a}_3$ does not influence the calculated tilt angles.

A tilt of type a^- around $\mathbf{a}_{\rm PC}$ is the angle between vector (O c′-O d′) and its projection in the xy plane. Similarly, an a^- tilt around $\mathbf{b}_{\rm PC}$ is the angle between vector (O a′-O b′) and its projection in the xy plane. Calculated values are shown in cells Y9 and Y10 in Fig. 5, with the mean value in cell Y11 (8.53°, 8.51° and 8.52°, respectively). The observed difference of 0.02° in calculated values results from an interplay of the deviation of $\gamma_{\rm PC}$ from 90° and the octahedral distortions.

The in-phase c^+ tilting causes the projections of the $\mathbf{a}_1$ and $\mathbf{a}_2$ octahedral vectors in the xy plane to be rotated away from pseudocubic axes $x_{\rm PC}$ and $y_{\rm PC}$ (Fig. 6). The two resulting tilt angles are given in cells Y12 and Y13 (8.82° and 8.87°), with the mean value in Y14 (8.84°).

The algorithms for calculating these tilt angles are described in §S3 of the supporting information, where reference is also made to their implementation in the *Excel* file in the supporting information.

e) Unit-cell volume $V_{\rm UC}$, polyhedral volumes V_B, V_A and volume ratio V_A/V_B are calculated in blocks P3:P4 and P6:P7. $V_{\rm UC} = \mathbf{a} \cdot \mathbf{b} \times \mathbf{c}$ and

$$V_B = \frac{1}{6}\begin{vmatrix} a_{1x} & a_{1y} & a_{1z} \\ a_{2x} & a_{2y} & a_{2z} \\ a_{3x} & a_{3y} & a_{3z} \end{vmatrix}.$$

The latter calculation method is facilitated by the centrosymmetry of the octahedron. Volume ratio V_A/V_B follows

[2] This activates a VBA macro, which calculates the values of structural parameters for the cells with a pink background. Although not included in the supporting information, the author is willing to supply an *xlsm* file containing VBA codes on request.

from these parameters as $[(V_{UC}/Z) - V_B]/V_B$ and V_A as $V_B(V_A/V_B)$.

f) **Parameters η_A and η_B** are likewise extracted from the core computational data (blocks R9:T11 and U9:W11) and defined in §2.6.

g) **Parameters L and ϕ** (block N18:19 with brown background) relate to the A ion positions and are independent of the anionic network. They are defined in §2.7.

2.4. Example Solver refinements

Initial insight into use of the Solver is gained here by addressing an issue relevant to the historical development of perovskite structural chemistry: the ability of different space groups to accommodate regular octahedra. A comparison is also made between tilt angles calculated as in point d) of §2.3 and the values yielded by commonly used approximations.

The five degrees of freedom required to define the regular octahedral form (see §2.2.1) result in the constraints a) $a_2 = a_1$; b) $a_3 = a_2$; c) $\theta_{23} = 90°$; d) $\theta_{31} = \theta_{23}$; and e) $\theta_{12} = \theta_{31}$. Since there are eight d.o.f. in total, two further constraints may be applied in the refinement. For example, it may be stipulated that the unit cell and the octahedral volumes remain unchanged: f) $V_{UC} = V_{UC,reference}$ and g) $V_B = V_{B,reference}$. The coding of these constraints in the Solver in shown in Fig. 7(*a*), whereby constraints f) and g) also refer to cells H3 and H4 in Fig. 5.

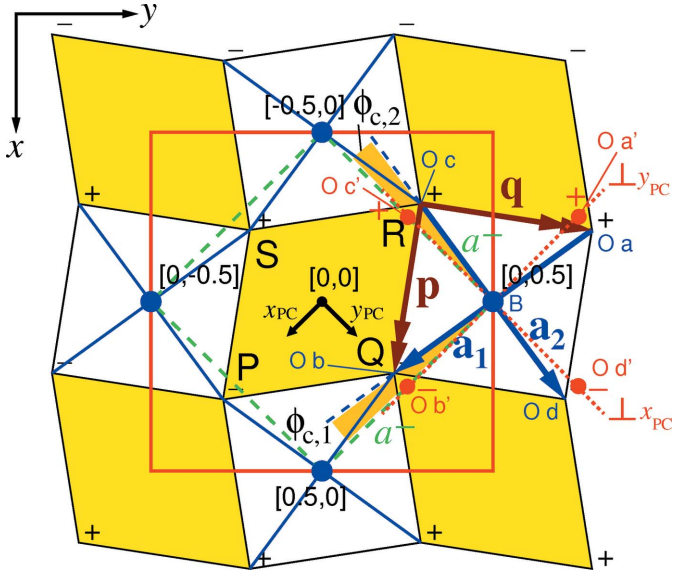

Figure 6
Tilted octahedra and basal parallelogram planes, *e.g.* PQRS, of AX_{12} polyhedra (in yellow) viewed along the orthorhombic z axis in space group *Pbnm*. The + and – signs in black denote z heights of the octahedral vertices relative to the z = 0 plane of the diagram. These are due to a^- tilting. Green dashed lines show the directions of pseudocubic axes x_{PC} and y_{PC}, the reference directions for the a^- tilting. Red dotted lines represent the perpendicular planes to the green dashed lines, which are projected as lines in the xy plane. Red circles lie above the red dotted lines at the same z height as the octahedral vertices O a to O d. They are denoted by O a′ to O d′ and result from the four projections (O a → O a′), (O b → O b′), (O c → O c′) and (O d → O d′). c^+ tilting causes the octahedra to be rotated about the orthorhombic z axis (or equivalently, the z_{PC} axis). The relevant tilt angles, $\phi_{c,1}$ and $\phi_{c,2}$, are shaded orange. (Vectors **p** and **q** are defined in §2.6.)

The end-point of this tightly defined refinement is shown in Fig. 7(*b*): a cubic PCRO of side length 3.9014 Å is generated, corresponding to a regular octahedron with perpendicular stalks. The values of the other structural parameters described in §2.3 appear in the cells with a light-blue background.

The crystal structures obtained by applying the same refinement conditions to reference structures in all the space groups are given in Table 3. The Solver constraints for the respective space groups are pre-programmed in the *Excel* file in the supporting information.

For space group $P4_2/nmc$, the obtaining of regular octahedra in tilt system $a^+a^+c^-$ is at variance with the conclusion of Howard & Stokes (1998). A resolution of this discrepancy is thought likely to depend on the observed interdependence of the coordinates of atoms O2 and O3 in the refined structure (Table 3), which implies a refinement into higher symmetry or pseudo-symmetry than $P4_2/nmc$.

The values of tilt angles below the dividing line in Table 3 serve to compare the values calculated by the method given in §2.3 and approximations for tilt angles used by other authors. Following an initial analytical treatment of perovskite tilt

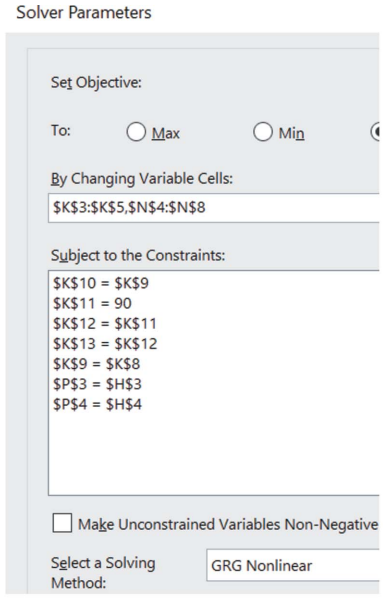

(*a*)

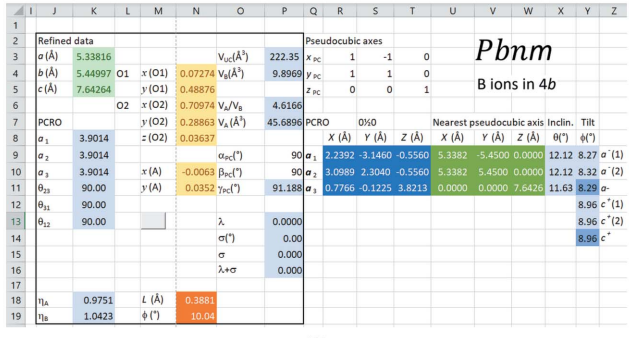

(*b*)

Figure 7
(*a*) Solver settings for generating regular octahedra in space group *Pbnm* with unchanged unit cell and octahedral volumes. (*b*) Results of the refinement.

Table 3
Summary of Solver refinements by space group corresponding to structures with regular octahedra.

The octahedral and unit-cell volumes are identical to those in the reference structures.

Space group	*Pbnm* (B: 4*b*)	*Pbnm* (B: 4*a*)	*Cmcm*	*Ibmm*	*P4/mbm*	$P4_2/nmc$	*I4/mcm*	$R\bar{3}c$
Reference system	$CaTiO_3$	$LaCr_{0.7}Ni_{0.3}O_3$	$NaNbO_3$ at 848 K	$BaPbO_3$ at 300 K	$NaNbO_3$ at 888 K	$CaMnO_3$	$CaTiO_3$ at 1523 K	$La(Cr_{0.2}Ni_{0.8})O_3$
Reference ICSD	162908	173471	192404	154038	280100	670342	162919	173475
a_1(refined) (Å)	3.9014	3.9535	3.9495	4.3480	3.9500	3.8074	3.9025	3.8952
a (Å)	5.33816	5.46101	7.85139	6.08315	5.56480	7.52285	5.47004	5.42241
b (Å)	5.44997	5.57887	7.85672	6.14899				
c (Å)	7.64264	7.73997	7.89355	8.60287	3.94998	7.43089	7.80495	13.49346
x(O1)	0.07274	0.57385	0.27596	0.05216	0	0.03909	0	0.55170
y(O1)	0.48876	0.49521	0	0	0	$-x$(O1)	0	0
z(O1)	$\frac{1}{4}$	$\frac{1}{4}$	0	$\frac{1}{4}$	$\frac{1}{2}$	$\frac{1}{4}$	$\frac{1}{4}$	$\frac{1}{4}$
x(O2)	0.70974	0.23308	0	$\frac{1}{4}$	0.22810	$\frac{1}{4}$	0.21650	
y(O2)	0.28863	0.26621	0.22407	$\frac{1}{4}$	0.72810	0.00306	0.71650	
z(O2)	0.03637	0.03692	0.00921	−0.02608	0	0.96043	0	
x(O3)			0.25921			$\frac{1}{4}$		
y(O3)			0.25096			*y*(O2)		
z(O3)			$\frac{1}{4}$			$-z$(O2) + $\frac{1}{2}$		
Method	§2.3	§2.3 a)	§2.3 b)	§2.3 d)		§2.3	§2.3 c)	§2.3
ϕ_a (°)	8.52	8.47 11.91		6.37 8.72		7.13		5.90
$\phi_{a,refined}$ (°)	8.29	8.33 11.80		5.92 8.39		8.89		5.90
ϕ_b (°)			2.11 4.15			6.02		
$\phi_{b,refined}$ (°)			2.12 2.11			8.89		
ϕ_c (°)	8.84	4.90 4.90	5.38 5.38		5.01	9.34	7.63 7.63	
$\phi_{c,refined}$ (°)	8.96	3.79 3.79	5.92 5.92		5.01	0.70	7.63 7.63	
θ_3 (°)		10.97		7.87				
$\theta_{3,refined}$ (°)		11.80		8.39				

angles by Megaw (1973), a more developed treatment according to space group was given by Kennedy, Prodjosantoso *et al.* (1999) as follows. The four parameterizations a) to d) here correspond to headers a) to d) in the row 'Method' in Table 3.

a) *Pbnm* (*B* ions in 4*a*): O2:$\left(\frac{1}{4}-u, \frac{1}{4}+v, w\right)$. $\phi_a = \arctan\left(4 \cdot 2^{\frac{1}{2}} \cdot w\right)$; $\phi_c = \arctan\left(2[u+v]\right)$.

b) *Cmcm*: O1: $\left(\frac{1}{4}+u_1, 0, 0\right)$; O2: $\left(0, \frac{1}{4}-v_2, w_2\right)$; O3: $\left(\frac{1}{4}+u_3, \frac{1}{4}+v_3, \frac{1}{4}\right)$.

$\phi_b = \arctan\left(2\left[u_3+w_2\right]\right)$; $\phi_c = \arctan\left(2[u_1+v_2]\right)$.

c) *I4/mcm*: O: $\left(\frac{1}{4}+u, \frac{3}{4}+u, 0\right)$. $\phi_c = \arctan(4u)$.

Mountstevens *et al.* (2003) augmented this set with a result for space group *Imma*, which upon resetting in *Ibmm*, is as follows:

d) *Ibmm*: O2: $(\frac{1}{4}, \frac{1}{4}, w)$. $\phi_a = \arctan\left(4 \cdot 2^{\frac{1}{2}} \cdot w\right)$.

This expression is equivalent to *Pbnm* with $u = v = 0$.

In general, the agreement between values generated in this work and approximations a) to d) above is satisfactory for the in-phase tilts, ϕ_c. Antiphase angles ϕ_a for space groups *Pbnm* and *Ibmm* show poorer agreement. In order to investigate whether this is a systematic discrepancy, the structural data of Kennedy, Prodjosantoso *et al.* (1999) for $CaTiO_3$ (*Pbnm*) at 1273 K were fed into the *Excel* program, yielding the following two sets of tilt values and inclination angles θ_3: $\phi_a = 6.53°$; $\phi_{a,refined} = 6.59°$; $\theta_3 = 8.92°$; $\theta_{3,refined} = 9.24°$. These are to be compared with the tilt values given by the Kennedy approximation: $\phi_a = 9.19°$; $\phi_{a,refined} = 9.24°$. These results and those in the *Pbnm* (B: 4*a*) and *Ibmm* columns of Table 3 lead to the following two conclusions: (1) The ϕ_a angles calculated by the method of §2.3 are systematically lower than those generated by the Kennedy approximation; (2) The Kennedy approximation generates exact values of inclination angle for refined structures with regular octahedra, *i.e.* $\theta_{3,refined}$, and not tilt angle ϕ_a as defined in this work.

In the case of *Cmcm*, good agreement for ϕ_a between §2.3 and Kennedy, Prodjosantoso *et al.* (1999) is obtained for regular octahedra in the refined structure, but not for the distorted octahedra in the unrefined structure.

A rationalization for the smaller values of ϕ_a generated by the method of §2.3 is that the inclination angle θ_3 of a regular octahedron will always be larger than an angle within a plane of projection perpendicular to a pseudocubic axis (Fig. 6). The former angle is generated by the approximations of Kennedy, Prodjosantoso *et al.* (1999) and the latter angle by the method of §2.3.

2.5. PCRO parameters, inclination angles and tilt systems with numbers of degrees-of-freedom by space group

Whether regular octahedra can be formed in a particular space group depends on whether the octahedra have sufficient degrees of freedom (d.o.f.). The number of d.o.f. defining the octahedral anionic network is N(UC) + $N(X)$, of which N(tilt) are used to define independent tilt angles. In $P4_2/nmc$ with irregular octahedra, the tilt system is $a^+b^+c^-$, *i.e.* N(tilt) = 3. For regular octahedra, this is reduced to $a^+a^+c^-$ with N(tilt) = 2. The parameter denoting the remaining d.o.f. available to construct the octahedra, N(PCRO), is equal to N(UC) + $N(X)$ − N(tilt) (Table 4). In space groups *Pbnm* and *Cmcm*, N(PCRO) values equal to six signify a capacity to form regular octahedra independently of the values of the two tilt angles. Although N(PCRO) is less than 6 in *Ibmm*, *I4/mcm*, *P4/mbm*

Table 4
Summary of inclination angles, PCRO parameters and degrees of freedom by space group.

Space group	*Pbnm*	*Cmcm*	*Ibmm*	*I*4/*mcm* and *P*4/*mbm*	$P4_2/nmc$	$R\bar{3}c$	$Pm\bar{3}m$
3-axis in equation (1)	*z*	–	*z*	*z*	*z*	–	–
Inclination angles	$\theta_1 \neq 0$	$\theta_1 \neq 0$	$\theta_1 = \theta_2 \neq 0$	$\theta_1 \neq 0$	$\theta_1 \neq 0$	$\theta_1 = \theta_2 = \theta_3 \neq 0$	$\theta_1 = \theta_2 = \theta_3 = 0$
	$\theta_2 \neq 0$	$\theta_2 \neq 0$		$\theta_2 \neq 0$	$\theta_2 \neq 0$		
	$\theta_3 \neq 0$	$\theta_3 \neq 0$	$\theta_3 \neq 0$	$\theta_3 = 0$	$\theta_3 \neq 0$		
PCRO parameter equalities			$a_1 = a_3$	$a_1 = a_2$		$a_1 = a_2 = a_3$	$a_1 = a_2 = a_3$
			$\theta_{23} = \theta_{12}$	$\theta_{23} = \theta_{31} = \theta_{12} = 90°$		$\theta_{23} = \theta_{31} = \theta_{12}$	$\theta_{23} = \theta_{31} = \theta_{12} = 90°$
Tilt system	$a^-a^-c^+$	$a^0b^-c^+$	$a^-a^-c^0$	$a^0a^0c^-$ and $a^0a^0c^+$	$a^+b^+c^-$ or $a^+a^+c^-$	$a^-a^-a^-$	$a^0a^0a^0$
N(UC)	3	3	3	2	2	2	1
N(*X*)	5	5	2	1	5	1	0
N(tilt)	2	2	1	1	2	1	0
N(PCRO)	6	6	4	2	5	2	1
N(*A*)	2	2	1	0	0	0	0
N(*B*)	0	0	0	0	0	0	0

and $R\bar{3}c$, this does not preclude the formation of regular octahedra, since the space group symmetry itself provides partial regularity: in *Ibmm*: $a_1 = a_2$ and $\theta_{23} = \theta_{31}$; in *I*4/*mcm* and *P*4/*mbm*: $a_1 = a_2$ with $\theta_{23} = \theta_{31} = \theta_{12} = 90°$; in $R\bar{3}c$: $a_1 = a_2 = a_3$ with $\theta_{23} = \theta_{31} = \theta_{12}$. In space group $P4_2/nmc$, the *N*(PCRO) value of less than 6 signifies that the two tilt angles in the refined structure will be interdependent.

The final two rows in Table 4 relate to the d.o.f. assigned to *A* and *B* cations. The structures associated with the *A* cations are discussed in §2.7, after the primary structures associated with the parameter *N*(tilt) have been considered in the following sub-section.

2.6. Additional anionic network parameters related to octahedral tilting

Since octahedral tilting *per se* is a secondary structural feature relative to the BX_6 octahedra, the primary structures resulting from this tilting necessarily concern the coordination of the *A* ions. It has long been customary to assume AX_8 polyhedra in $GdFeO_3$-type perovskites such as $CaTiO_3$ in space group *Pbnm* (Liu & Liebermann, 1993). Mitchell & Liferovich (2004), adopting the perspective of coordination chemistry, reported an increase in coordination number from 8 to 9 with *x* in the solid solution series $Ca_{1-x}Na_xTi_{1-x}Ta_xO_3$. Mitchell (2002*b*) states generally that coordination numbers of 8, 9, 10 and 12 are possible, and calculates as an example the volume of uncoordinated space in $SrZrO_3$ (*I*4/*mcm*) as 8.7%. This is the difference between V_A, the volume assigned to AX_{12} polyhedra from volume filling with BX_6 octahedra, and the volume of a more appropriate AX_8 polyhedron, $V(AX_8)$.

From a functional viewpoint, the AX_8 polyhedra in tilted perovskites provide scaffolding to support the eight octahedral faces of the full AX_{12} polyhedra. In *Pbnm*, the inner AX_8 polyhedron is formed by the top and bottom parallelogram AX_{12} faces and four vertical struts (Fig. 8).

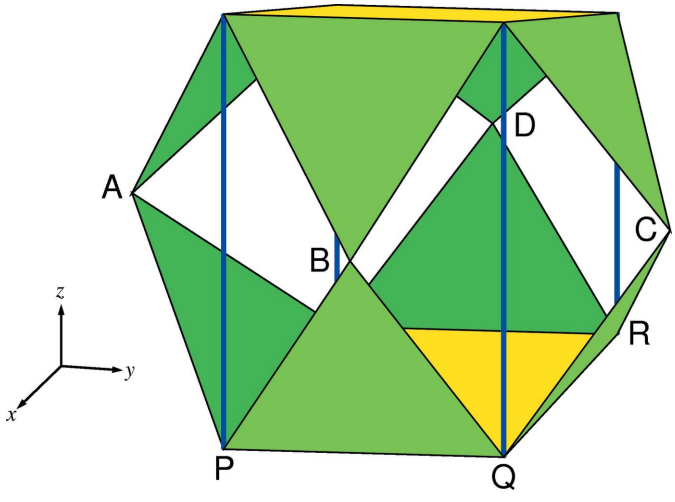

Figure 8
AX_8 and AX_{12} polyhedra in space group *Pbnm*. The two opposite, yellow parallelogram faces are joined by vertical blue struts to form AX_8 polyhedra. The eight green faces are shared with BX_6 octahedra.

It is now appropriate to interpret Fig. 6 in terms of the effect of octahedral tilting on *A*-ion coordination. The c^+ tilting causes parallelograms PQRS to be formed instead of rectangles, with a concomitant reduction in area *A*(*PQRS*). The a^- tilting, by comparison, leads to equal and opposite displacements of vertices *P*, *Q*, *R* and *S* along *z* (denoted by + and −). The volume contributions made by plane PQRS and the other five faces of the AX_8 polyhedron to $V(AX_8)$ are not affected by this tilting, since changes brought about by the equal and opposite displacements relative to the centre-of-symmetry at [0,0,0] cancel one another out.[3] The mirror plane through A, B, C and D in all space groups with c^+ tilting means that the horizontal positions, in this case the *x* and *y* coordinates of the bottom and top parallelograms in Fig. 8, are identical. It follows that the formula $V(AX_8) = A(PQRS)(c/2)$ could be used, since the centres of both parallelograms are separated by *c*/2 in all space groups with in-phase *c*-axis tilting apart from *P*4/*mbm*, where the separation is *c*. In space groups $P4_2/nmc$ and *I*4/*mcm*, to which anti-phase, c^- tilting applies, the same formula is valid, since the mean cross-section $\perp z$ is *A*(*PQRS*).

[3] Polyhedral volume = $\frac{1}{3}\sum A_i h_i$. A_i is area of face; h_i is perpendicular distance from face to common apex inside polyhedron.

Table 5
Analytical expressions for structural parameters η_A and η_B to quantify $c^{\pm}$ and $a^{\pm}b^{\pm}$ tilting.

Space group	N(tilt)	η_A	η_B
Pbnm (*B* in 4*b*)	2	$(1 - [3 - 4x(\mathrm{O2})][4y(\mathrm{O2}) - 1])$	$4(\mathbf{a}_3 \cdot \mathbf{a}_1 \times \mathbf{a}_2) \times \left(c\begin{vmatrix} a_{2x} + a_{1x} & a_{2y} + a_{1y} \\ a_{2x} - a_{1x} & a_{2y} - a_{1y} \end{vmatrix}\right)^{-1}$
Pbnm (*B* in 4*a*)	2	$([1 + [4x(\mathrm{O2}) - 1][4y(\mathrm{O2}) - 1])$	As for *Pbnm* (*B* in 4*b*)
Cmcm	2	$16x(\mathrm{O1})y(\mathrm{O2})$	As for *Pbnm* (*B* in 4*b*)
Ibmm	1	1	As for *Pbnm* (*B* in 4*b*)
*P*4/*mbm*, *I*4/*mcm*	1	$8x(\mathrm{O2})(1- 2x(\mathrm{O2}))$	1
$P4_2/nmc$	3	2*a*,2*b*: $4(-\frac{3}{2} + 2y(\mathrm{O3}))(\frac{1}{2} + 2y(\mathrm{O2}))$ 4*d*: $4(\frac{5}{2} - 2y(\mathrm{O3}))(\frac{1}{2} - 2y(\mathrm{O2}))$	As for *Pbnm* (*B* in 4*b*)
$R\bar{3}c$	1	$4x(\mathrm{O})(1 - x(\mathrm{O}))$	–

Since the $c^{\pm}$ component of the tilting is solely responsible for the reduction in $A(PQRS)$ and $V(AX_8)$, the converse applies that $A(PQRS)$ quantifies the extent of this tilting. Without $c^{\pm}$ tilting, $A(PQRS)$ would be equal to one quarter of the unit cell cross-sectional area, *i.e.* $(ab)/4$ in crystal systems with perpendicular x and y axes. A dimensionless coefficient η_A to quantify the amount of $c^{\pm}$ tilting may therefore be defined as follows.

$$\eta_A = \frac{A(PQRS)}{(ab)/4} \tag{5}$$

Although the b^- tilting about the x_{PC} and y_{PC} axes in *Pbnm*, more generally the $a^{\pm}b^{\pm}$ tilting component when applied to all space groups, does not affect $V(AX_8)$, it does affect V_B. For a given perovskite compound with unit-cell cross-section ab, this tilting allows larger V_B values than would otherwise have been the case. The greater the degree of tilting, the larger the V_B value. A dimensionless coefficient η_B to quantify this is given by relating V_B to the volume of an upright, untilted octahedron of equal basal area in xy projection, $V_{B,\mathrm{ref}}$. The in-plane components of vectors **p** and **q** in Fig. 6 define the waist of this octahedron of perpendicular height $c/2$. These depend in turn on PCRO vectors $\mathbf{a}_1$ and $\mathbf{a}_2$.

$$\mathbf{p} = \frac{1}{2}\begin{pmatrix} a_{2x} + a_{1x} \\ a_{2y} + a_{1y} \\ 0 \end{pmatrix}$$

and

$$\mathbf{q} = \frac{1}{2}\begin{pmatrix} a_{2x} - a_{1x} \\ a_{2y} - a_{1y} \\ 0 \end{pmatrix}.$$

$$\eta_B = \frac{V_B}{V_{B,\mathrm{ref}}} \tag{6}$$

In the presence of $a^{\pm}b^{\pm}$ tilting, $\eta_B > 1$. V_B is calculated as one-sixth of the volume of the PCRO and $V_{B,\mathrm{ref}}$ as twice the volume of a right pyramid of height $c/4$ with parallelogram base of area

$$\begin{vmatrix} p_x & p_y \\ q_x & q_y \end{vmatrix},$$

i.e.

$$\frac{1}{3}\cdot\frac{c}{2}\begin{vmatrix} p_x & p_y \\ q_x & q_y \end{vmatrix}.$$

Analytical expressions for η_A and η_B are quoted in Table 5. The form of η_B is similar for all space groups, and η_A can generally be traced back to simple expressions involving fractional coordinates. Particularly significant are the fixed, limiting values of $\eta_A = 1$ and $\eta_B = 1$ in space groups *Ibmm* and *I*4/*mcm*, respectively. These govern the sequence of phase transitions in series with increasing V_A volume (see §3.1). The corresponding derivations are in §S4 of the supporting information, along with diagrams of the $c^{\pm}$ and $a^{\pm}b^{\pm}$ tilt patterns determining η_A and η_B, respectively. These parameters are also calculated in the *Excel* datafile in the supporting information.

Since $c^{\pm}$ tilting reduces $V(AX_8)$ and therefore V_A, whereas $a^{\pm}b^{\pm}$ tilting increases V_B, use of V_A/V_B as an indicator of the overall degree of tilting is vindicated. By using parameters η_A and η_B to quantify the tilting, which are simply calculated, the difficulties of defining and calculating tilt angles unequivocally can be circumvented. As may be inferred from the complexity of Fig. 6 and the comparison of calculated tilt angles in the lower part of Table 3, this could be seen as an advantage.

2.7. *A* cation positions

In earlier work on the parameterization of centrosymmetric perovskites (Thomas, 1998), difficulties were experienced in fixing the positions of the A ions by reference to their coordinating X ions in the AX_{12} polyhedra. However, subsequent work by Magyari-Köpe *et al.* (2001, 2002) demonstrated that their positions could be treated as a function of the V_A/V_B ratio.

The essential objective is to quantify the small displacements from geometrically regular positions [0, 0] and $[\frac{1}{2}, \frac{1}{2}]$ in the relevant plane of projection (Fig. 9). The parameterization applied here is limited to a transformation to polar coordi-

Table 6
Structural parameters for two solid solutions spanning space group *Ibmm* at room temperature.

Composition	ICSD	Space group	η_A	η_B	V_A (Å^3)	V_B (Å^3)	V_A/V_B	λ	σ
$SrSnO_3$	190602	*Pbnm*	0.9847 (1)	1.0313 (3)	54.181 (5)	11.454 (4)	4.730 (2)	0.0023 (4)	0.0104 (8)
$Sr_{0.8}Ba_{0.2}SnO_3$	190611	*Pbnm*	0.9935 (2)	1.0236 (3)	55.10 (6)	11.42 (1)	4.824 (2)	0.0052 (7)	0.0195 (9)
$Sr_{0.6}Ba_{0.4}SnO_3$	190610	*Ibmm*	1	1.0147 (2)	56.02 (7)	11.40 (2)	4.913 (1)	0.0004 (3)	0.0091 (8)
$Sr_{0.4}Ba_{0.6}SnO_3$	190609	*I*4/*mcm*	0.9960 (1)	1	56.9 (1)	11.43 (2)	4.9758 (6)	0.0000 (4)	0
$Sr_{0.2}Ba_{0.8}SnO_3$	190608	*Pm*$\bar{3}$*m*	1	1	57.52 (8)	11.50 (2)	5	0	0
$BaSnO_3$	190601	*Pm*$\bar{3}$*m*	1	1	58.071 (4)	11.6142 (8)	5	0	0
$SrHfO_3$	89383	*Pbnm*	0.9856 (6)	1.034 (1)	55.64 (2)	11.79 (2)	4.719 (8)	0.003 (2)	0.013 (1)
$Sr_{0.8}Ba_{0.2}HfO_3$	55746	*Pbnm*	0.996 (2)	1.029 (4)	57.16 (6)	11.89 (6)	4.81 (3)	0.033 (6)	0.058 (9)
$Sr_{0.6}Ba_{0.4}HfO_3$	55747	*Ibmm*	1	1.026 (1)	57.97 (1)	11.96 (1)	4.848 (7)	0.0058 (5)	0.039 (3)
$Sr_{0.4}Ba_{0.6}HfO_3$	55748	*I*4/*mcm*	0.98755	1	58.88 (1)	11.95 (1)	4.926 (5)	0.0013 (2)	0
$Sr_{0.2}Ba_{0.8}HfO_3$	55749	*Pm*$\bar{3}$*m*	1	1	59.7948 (9)	11.9590 (2)	5	0	0
$BaHfO_3$	–	*Pm*$\bar{3}$*m*	1	1	60.2909 (4)	12.0582 (1)	5	0	0

nates L and ϕ in *Pbnm* [Fig. 9(*a*)], whereby L is twice the displacement of an individual ion. In space group *Cmcm*, two independent lengths, L_1 and L_2, apply [Fig. 9(*b*)]. These displacements are either along one axis or non-existent in the other space groups.

3. Analysis of structures at variable temperature and chemical composition

The structural parameters defined in §2 are used here to characterize the sequences of phase transitions observed with increasing temperature and varying chemical composition in centrosymmetric perovskites. Li *et al.* (2004) identified the following commonly occurring sequence with increasing temperature or mean *A* ion radius: *Pbnm* → *Ibmm* → *I*4/*mcm* → *Pm*$\bar{3}$*m*. This applies to $Sr_{1-x}Ba_xHfO_3$ and $Sr_{1-x}Ba_xZrO_3$ perovskites (Kennedy *et al.*, 2001), as well as to the systems $Sr_{1-x}Ba_xSnO_3$ and $Ca_{1-x}Sr_xSnO_3$ (Mountstevens *et al.*, 2003). Identification of the intermediate *Ibmm* phase was significant, as it had previously been regarded as rare (Kennedy *et al.*, 2001). The temperature range of stabilization of this phase is highly variable, with values greater than 570 K in $BaPbO_3$ (Fu *et al.*, 2007), of 140 K in $SrRuO_3$ (Kennedy *et al.*, 2002), 90 K in $SrHfO_3$ (Li *et al.*, 2004) and less than 20 K in $SrRhO_3$ (Kennedy *et al.*, 2004). It is characterized by a fixed value of parameter η_A equal to one (Table 5).

A second sequence was identified by Ahtee & Darlington (1980) for $NaTaO_3$: *Pbmn* → *Cmcm* → *P*4/*mbm* → *Pm*$\bar{3}$*m*, with further structural work by Kennedy, Prodjosantoso *et al.* (1999) reporting transition temperature ranges of 738–753 K, 823–863 K and 883–913 K. More recently, Mitchell *et al.* (2014) reported the same series of phase symmetries for the mineral lueshite, $NaNbO_3$.

Both sequences are characterized by an increasing V_A/V_B ratio with T or x, which may be attributed either to a larger volume expansion coefficient of V_A relative to V_B or to a compositionally induced expansion of the *A*-site volume relative to the *B* site. The term '*A*-ion perturbation' may be applied in both cases, since a change in the *A*-site geometry is the dominant driving force causing the whole structure to respond.

A solid solution series with a rising V_A/V_B ratio brought about by reducing V_B has been established by Yang (2008) for

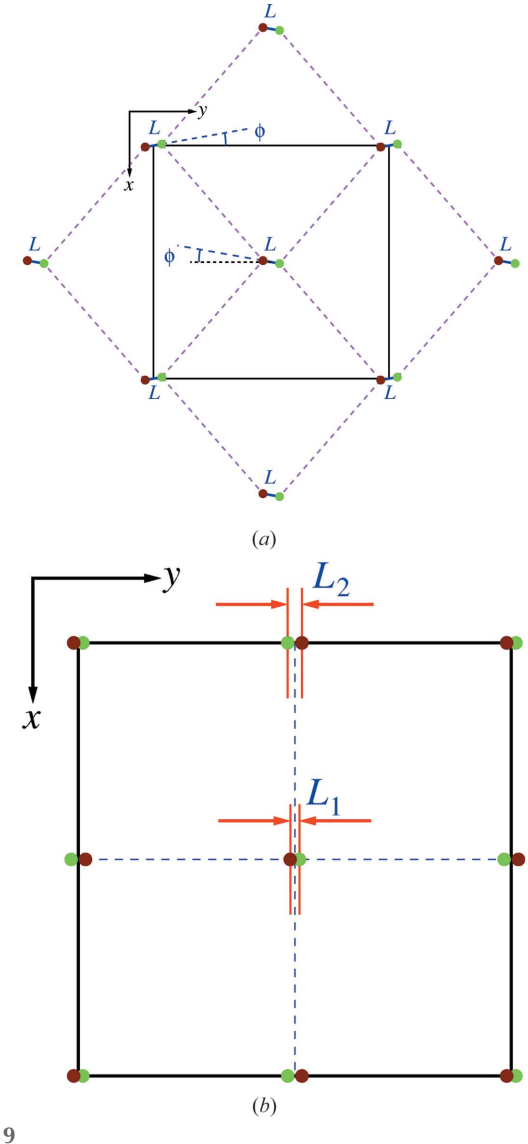

Figure 9
A cation positions in space groups (*a*) *Pbnm* and (*b*) *Cmcm* in 2D projection. Green circles: height $+\frac{1}{4}$; brown circles: height $-\frac{1}{4}$. A network with dashed lines is shown in (*a*).

Table 7
Focus on the *Cmcm* phases of $NaTaO_3$ and $NaNbO_3$ with comparative data for neighbouring *Pbnm* and *P*4/*mbm* phases.

Compound	ICSD	Temperature (K)	V_A/V_B	η_{A1}	η_{A2}	η_B	Reference
Pbnm							
$NaTaO_3$	150430	293	4.74 (2)	0.988 (2)		1.032 (3)	Mitchell & Liferovich (2004)
$NaNbO_3$	192400	293	4.802 (5)	0.9868 (6)		1.0206 (6)	Mitchell *et al.* (2014)
Cmcm							
$NaTaO_3$	280099	803	4.899 (2)	0.987 (3)	0.994 (3)	1.0076 (2)	Darlington & Knight (1999)
$NaTaO_3$	241445	778	4.891 (2)	1.002 (2)	0.977 (2)	1.0076 (2)	Knight & Kennedy (2015)
$NaTaO_3$†	239691	783	4.889 (3)	0.991 (5)	0.989 (5)	1.0087 (3)	Arulnesan *et al.* (2016)
$NaNbO_3$	192404	848	4.928 (3)	1.051 (3)	0.933 (3)	1.0041 (4)	Mitchell *et al.* (2014)
$NaNbO_3$	192405	873	4.940 (2)	1.063 (3)	0.924 (3)	1.0033 (3)	Mitchell *et al.* (2014)
*P*4/*mbm*							
$NaTaO_3$	88377	843	4.945 (1)	0.9907 (2)			Kennedy, Prodjosantoso *et al.* (1999)
$NaNbO_3$	192406	898	4.9687 (7)	0.9948 (1)		1	Mitchell *et al.* (2014)

† Doped with 1 mol% K.

$LaCr_{1-x}Ni_xO_3$ at room temperature. Upon increasing x from 0 to 0.7, a *Pbnm* → $R\bar{3}c$ phase transition is observed. In this case, a *B*-ion perturbation is being applied.

3.1. *x*- and *T*-series with *A*-ion perturbations

3.1.1. $Sr_xBa_{1-x}SnO_3$ and $Sr_xBa_{1-x}HfO_3$. Table 6 contains structural parameters calculated from the refinements of Mountstevens *et al.* (2003) for the solid solution series $Sr_xBa_{1-x}SnO_3$ and of Li *et al.* (2004) for the $Sr_xBa_{1-x}HfO_3$ series.

On reading Table 6 from top to bottom, values of V_A confirm that the increasing mean *A*-ion radius is the principal driving force for the structural changes in both systems. V_A rises by 7.2% between $x = 0$ and $x = 1$ in the tin-containing and by 8.4% in the hafnium-containing series. Furthermore, the larger ionic radius of Hf^{4+} compared to Sn^{4+} in sixfold coordination [0.71 *cf.* 0.69 Å; Shannon (1976)] causes the V_A value at a given Sr:Ba ratio to be systematically larger in the system with hafnium as *B* ion. By comparison, the volume of the *B* site increases by 1.4% between $x = 0$ and $x = 1$ in the tin-containing series compared system compared to 2.3% in the hafnium series. The following ranges of the V_A/V_B parameter

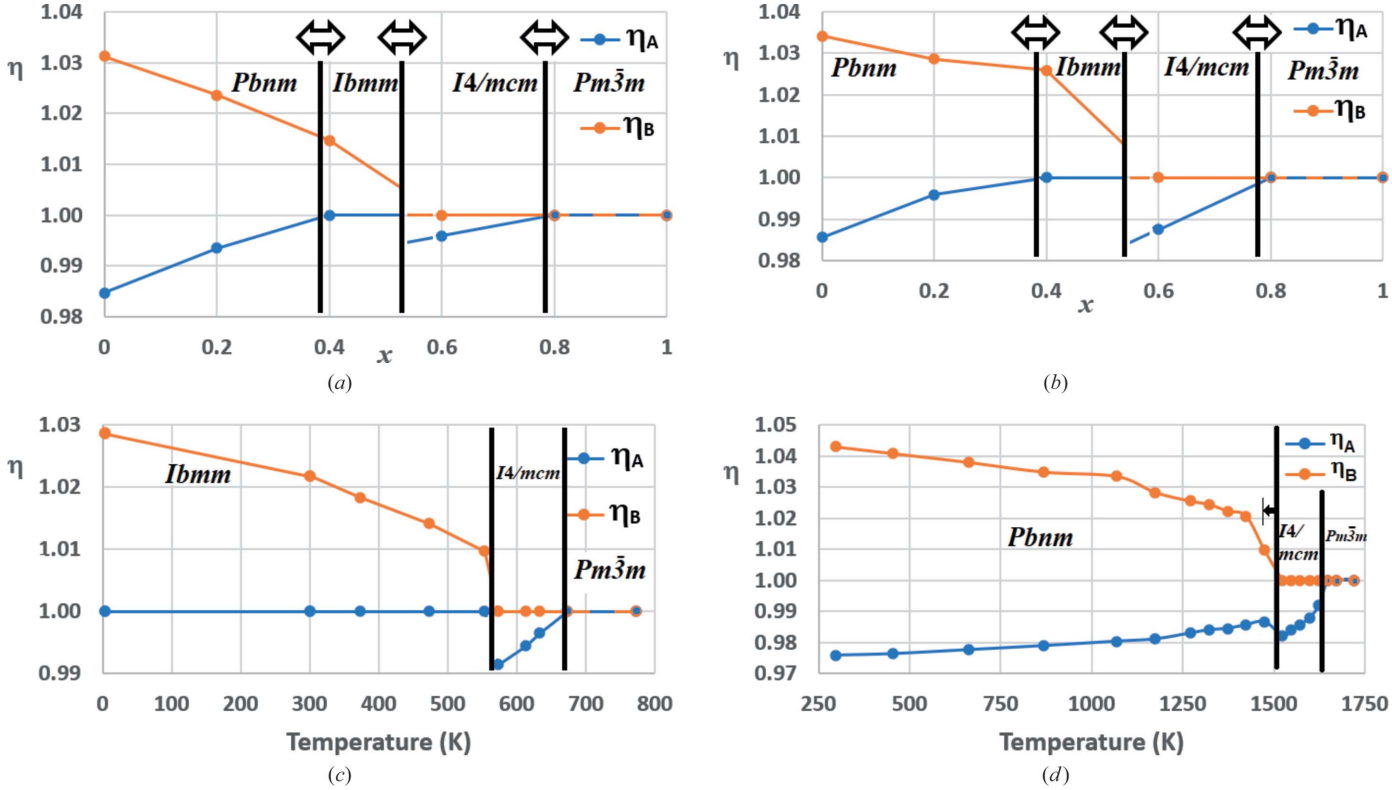

Figure 10
Characterization of phase transitions in terms of tilt-related parameters η_A and η_B: (*a*) $Sr_xBa_{1-x}SnO_3$, (*b*) $Sr_xBa_{1-x}HfO_3$, (*c*) $BaPbO_3$, (*d*) $CaTiO_3$. Circles denote experimentally determined points, which are joined by straight lines. Arrows signify limited flexibility in the positions of the phase transitions.

span the *Ibmm* phase in the two systems: $4.824 < V_A/V_B < 4.976$ and $4.81 < V_A/V_B < 4.926$.

The variation of parameters η_A and η_B with x reveals the mechanisms behind the *Pbnm* → *Ibmm* and *Ibmm* → *I*4/*mcm* phase transitions in these series [Figs. 10(*a*) and 10(*b*)].

Reading these two diagrams from left to right, the *Pbnm* → *Ibmm* transition is triggered by η_A reaching the limiting value of 1 whilst η_B is still > 1. The range of stability of the *Ibmm* phase is determined by the x value at which η_B becomes equal to 1, whereupon a phase transition to *I*4/*mcm* takes place. The diagrams suggest that the approach of η_A to 1 takes place continuously at the *Pbnm*–*Ibmm* boundary. By comparison, the *Ibmm*–*I*4/*mcm* boundary is characterized by a discontinuous step in η_B down to 1. Also characteristic of the latter boundary is a fall in η_A to a value less than 1. This may be understood by considering that η_A and η_B can only both be equal to one in the aristotype *Pm*$\bar{3}$*m* phase. However, at the start of the range of stability of the *I*4/*mcm* phase, V_A/V_B has not reached the limiting value of 5. The transition from *I*4/*mcm* to *Pm*$\bar{3}$*m* takes place as soon as V_A has increased sufficiently for this V_A/V_B limit to be reached.

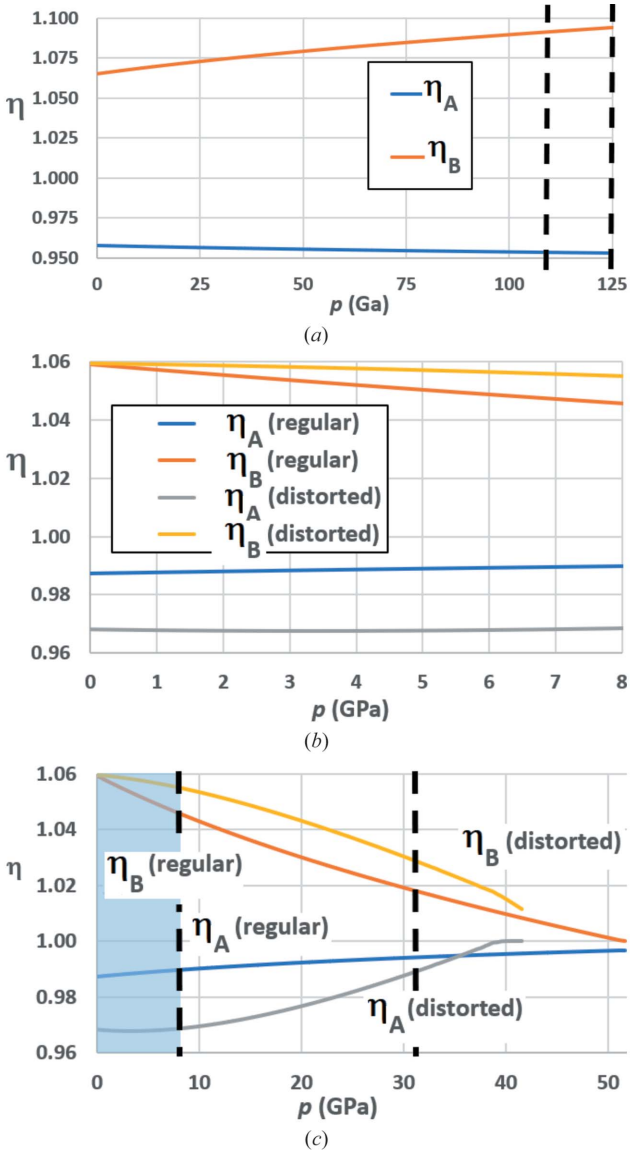

Figure 11
Simulations of $MgSiO_3$ and $YAlO_3$ in terms of η_A and η_B. (*a*) $MgSiO_3$ with regular octahedra up to p = 125 GPa; (*b*) comparison of $YAlO_3$ with regular and distorted octahedra up to p = 8 GPa; (*c*) Extrapolation of $YAlO_3$ with regular and distorted octahedra up to p = 52 GPa. Dashed lines indicate pressures for which structural data are quoted in Table 10.

3.1.2. $BaPbO_3$. The above rationalization can be transferred without modification to series where temperature is responsible for an increasing V_A volume. For example, the *Ibmm* phase is stabilized over a wide temperature range in $BaPbO_3$ perovskites, these being of technological relevance due to superconductivity in the Ba-Pb-Bi-O system. Following earlier structural refinements by Moussa *et al.* (2001) and Ivanov *et al.* (2001) in the monoclinic space group *C*2/*m* on cooling and at room temperature, respectively, Fu *et al.* (2005) interpreted this monoclinic distortion as probably due to twinning. They also provided four structural refinements in *Ibmm* at room temperature and at 4.2 K. Upon heating, Fu *et al.* (2007) reported phase changes to tetragonal *I*4/*mcm* and thereafter to *Pm*$\bar{3}$*m* at approximate temperatures of 573 and 673 K respectively. Fig. 10(*c*) is generated from experimental points calculated from the structural refinements of Fu *et al.* (2005, 2007). The absence of *Pbnm* symmetry in $BaPbO_3$ can be ascribed to the V_A/V_B ratio remaining above 4.8320 (8) over the temperature range from 4.2 K to 773 K, this being higher than the threshold values of 4.81 and 4.824 noted in §3.1.1 for *Ibmm* symmetry. This interpretation is supported by the stabilization of the strontium compound $SrPbO_3$ in *Pbnm* (Fu & Ijdo, 1995). The calculated V_A/V_B value here is significantly lower, at 4.418 (2).

Despite the absence of a *Pbnm* phase in $BaPbO_3$, Fig. 10(*c*) shows that the *Ibmm* → *I*4/*mcm* transition is also governed by discontinuous jumps in η_B to 1 and η_A to less than 1, as in Figs. 10(*a*) and 10(*b*). The approach to the aristotype phase follows the same principles as noted earlier.

3.1.3. $CaTiO_3$. The mineral perovskite, $CaTiO_3$, has not been observed in space group *Ibmm*, although it exists in *Pbnm* at room temperature (Sasaki *et al.*, 1987) and at temperatures up to 1373 K (Liu & Liebermann, 1993). Redfern (1996) paved out the sequence of phase transitions at yet higher temperatures through *I*4/*mcm* to and *Pm*$\bar{3}$*m* aristotype, reporting transition temperatures of 1373–1423 K and at ∼1523 K. Although Kennedy, Howard & Chakoumakos (1999) subsequently raised the possibility of an orthorhombic *Cmcm* structure being stabilized at around 1380 K, this was refuted by Ali & Yashima (2005), who later generated the nineteen structural refinements upon which the experimental points of Fig. 10(*d*) are based (Yashima & Ali, 2009). It is logical that no intermediate phase of symmetry *Ibmm* is formed with increasing temperature, since η_A remains significantly below one over the whole *Pbnm* range. This means that the degree of AO_8 expansion induced thermally is smaller than the compositionally induced AO_8-expansion analysed in §3.1.1. Stabilization of the *Pbnm* phase is curtailed by η_B falling to 1 at the *Pbnm*–*I*4/*mcm* boundary. After the

Table 8
Structural data relevant to the $Pbnm \rightarrow R\bar{3}c$ transition at $x \sim 0.7$ in $LaCr_{1-x}Ni_xO_3$.

Composition	ICSD	Space group	η_A	η_B	$\langle\phi_c\rangle$ (°)	$\langle\phi_a\rangle$ (°)	$(\langle\phi_a\rangle + \langle\phi_c\rangle)/2$ (°)	V_A (Å^3)	V_B (Å^3)	V_A/V_B
$x = 0$	173469	*Pbnm*	0.9925 (1)	1.0355 (7)	5.02 (3)	8.5 (2)	6.78 (8)	48.38 (1)	10.182 (7)	4.751 (4)
$x = 0.3$	173471	*Pbnm*	0.9836 (4)	1.0278 (9)	8.67 (5)	5.4 (2)	7.05 (8)	48.28 (1)	10.178 (9)	4.744 (5)
$x = 0.6$	173472	*Pbnm*	0.9900 (1)	1.0301 (8)	6.13 (4)	6.5 (2)	6.32 (10)	48.388 (9)	10.152 (8)	4.766 (5)
$x = 0.7$	173473	*Pbnm*	0.9983 (3)	1.0254 (5)	6.36 (3)	4.64 (9)	5.50 (5)	48.204 (9)	9.956 (6)	4.841 (3)
$x = 0.7$	173474	$R\bar{3}c$	0.9891 (1)			5.97 (3)		47.453 (5)	9.867 (4)	4.809 (2)
$x = 0.8$	173475	$R\bar{3}c$	0.9893 (2)			5.90 (5)		47.414 (7)	9.850 (5)	4.814 (3)
$x = 0.9$	173476	$R\bar{3}c$	0.9897 (1)			5.79 (3)		47.29 (1)	9.810 (4)	4.820 (2)
$x = 1$	173477	$R\bar{3}c$	0.9900 (1)			5.72 (3)		46.778 (3)	9.696 (2)	4.825 (1)

temperature of this phase transition has been reached, the overall expansion of the unit cell allows the volumetric requirements of the TiO_6 octahedron to be satisfied without a^- tilting in space group $I4/mcm$. The remaining tilting allows further comparatively greater AO_8 expansion with increasing temperature up to the temperature of the phase transition to $Pm\bar{3}m$.

In all four series upon which Fig. 10 is based, the changes in tilt systems taking place at the phase transitions, these being critical events, are largely determined by the systematic changes in tilt angles taking place over wide compositional or temperature ranges. Parameters η_A and η_B are ideally suited for encapsulating these changes.

3.1.4. $NaTaO_3$ and $NaNbO_3$. These compounds provide an experimental basis for assembling the factors governing stabilization of the *Cmcm* phase, and more widely, the progression from *Pbnm* to $Pm\bar{3}m$ via *Cmcm* and *P*4/*mbm* instead of *Ibmm* and *I*4/*mcm*. *I*4/*mcm* and *P*4/*mbm* structures are very similar, the only difference being anti-phase or in-phase *c* axis tilting, respectively. Furthermore, structural parameters V_A/V_B, η_A and η_B cannot discriminate between these two structures. It is therefore appropriate to regard *Cmcm* and *Imma*, in the first instance, as alternative precursor phases to a generic phase of symmetry *I*4/*mcm* or *P*4/*mbm*.

An analysis of the phases of *Cmcm* symmetry in terms of V_A/V_B, η_A and η_B within these two compounds is given in Table 7.

The definitive characteristic of the *Cmcm* phase is the proximity of η_B values to one in Table 7. This parameter has much larger values in the *Ibmm* phase, with η_B values greater than 1.03 observed [see Table 6 and Figs. 10(*a*), 10(*b*) and 10(*c*)]. This difference is due to there being only one tilt of type $a^{\pm}b^{\pm}$ in *Cmcm*, compared to two in *Ibmm* (see §S4 of the supporting information). Values of η_B close to one confirm *Cmcm* as a precursor to an *I*4/*mcm* or *P*4/*mbm* phase, in which η_B is exactly equal to one. The existence of *Cmcm* symmetry in $CaTiO_3$ at ∼1380 K, as proposed by Kennedy, Howard & Chakoumakos (1999), is indeed possible, since η_B is close to one at this temperature.

Also to be noted in Table 7 is the splitting of η_A values made possible by there being two symmetry-independent *A* sites in *Cmcm*. Geometry simply requires a mean value $\langle\eta_A\rangle = (\eta_{A1} + \eta_{A2})/2$ of less than one. This splitting is considerably more marked in $NaNbO_3$. The ability for the lower η_A value to be significantly less than one could go some way towards rationalizing the phase coexistence of *Pbnm* and *Cmcm* phases at room temperature observed in $NaTaO_3$ by Knight & Kennedy (2015). A further contributory factor towards stabilization of *Cmcm* in 1 mol% K-doped samples of $NaTaO_3$ at room temperature (Arulnesan *et al.*, 2016) could be preferential occupation of the sites with higher η_A value by the larger potassium ions, *i.e.* a partial ordering.

It is speculated that the proximity of η_B to one in *Cmcm* is conducive to a to a higher temperature phase transition to *P*4/*mbm*, whereas the sudden fall in η_B within *Ibmm* or *Pbnm* phases observed in Figs. 10(*a*)–10(*d*) favours a transition to *I*4/*mcm*.

3.2. *X*-series with *B*-ion perturbations

Calculated structural parameters for the $LaCr_{1-x}Ni_xO_3$ solid solution series (Yang, 2008) are given in Table 8.

Unlike the structures perturbed by *A* ions, the variation in η_A and η_B parameters is small and also unsystematic for structures in space group *Pbnm*. There is no tendency of either parameter to approach one. The expected cross-correlations between parameter pairs $\eta_A \leftrightarrow \phi_c$ and $\eta_B \leftrightarrow \phi_a$ are observed within the *Pbnm* phase field: the greater the magnitude of the deviations of η_A and η_B from one, the larger the $\langle\phi_c\rangle$ and $\langle\phi_a\rangle$ angles. The ϕ_a tilt angle falls to 4.64° and the mean tilt angle $(\langle\phi_a\rangle + \langle\phi_c\rangle)/2$ to 5.50° in *Pbnm* just before the phase transition, with ϕ_a rising to 5.97° in the $R\bar{3}c$ phase at $x = 0.7$. A gradual reduction in ϕ_a to 5.72° is observed up to $x = 1$, this still being a stable rhombohedral phase far from a transition to the cubic aristotype. The gradual fall in V_B with x is consistent with the smaller ionic radius of Ni^{3+} compared to Cr^{3+} (Shannon, 1976) and is responsible for the systematic increase in V_A/V_B with x, which peaks at 4.841 in *Pbnm* before the phase transition to $R\bar{3}c$ and falls to 4.809 thereafter. The $Pbnm \rightarrow R\bar{3}c$ transition is examined further in §4.4.

4. Modelling the structural variation of *Pbmn* perovskites with increasing pressure

The structures adopted by perovskites under increasing hydrostatic pressure rest on the different compressibilities of the AX_{12} and BX_6 polyhedra (Angel *et al.*, 2005), such that the volume ratio V_A/V_B may either increase or decrease. In

Table 9
Validation of Birch–Murnaghan (B-M) constants for use at pressures of up to to ∼125 GPa†.

Method/calculation type	p (GPa)	a (Å)	b (Å)	c (Å)	V_{uc} (Å^3)
Murakami XRD	109	4.325	4.579	6.308	124.9
Murakami MD	109	4.403	4.574	6.410	129.1
Extrapolated B-M	109	4.365	4.559	6.315	125.7
Fiquet synchrotron XRD	40.66	–	–	–	143.26
Extrapolated B-M	40.71	4.571	4.743	6.606	143.22

† V_{uc}: unit-cell volume.

Table 10
Crystallographic and structural parameters generated in the simulations of $MgSiO_3$ and $YAlO_3$.

Compound	$MgSiO_3$	$MgSiO_3$	$YAlO_3$	$YAlO_3$	$YAlO_3$	$YAlO_3$
Pressure (GPa)	109	125	8	8	31.5	31.5
Octahedra	Regular	Regular	Regular	Distorted	Regular	Distorted
a (Å)	4.3649	4.3278	5.1285	5.1285	5.0308	5.0308
b (Å)	4.5592	4.5263	5.2443	5.2443	5.0751	5.0751
c (Å)	6.3151	6.2628	7.2899	7.2899	7.1349	7.1349
x(O1)	0.1067	0.1083	0.0756	0.0810	0.0470	0.0604
y(O1)	0.4780	0.4775	0.4925	0.4810	0.4965	0.4934
x(O2)	0.6936	0.6933	0.7241	0.7054	0.7309	0.7241
y(O2)	0.3017	0.3019	0.2748	0.2940	0.2687	0.2758
z(O2)	0.0533	0.0542	0.0378	0.0420	0.0235	0.0295
γ_{PC} (°)	92.49	92.57	91.28	91.28	90.50	90.50
V_A (Å^3)	25.439	24.816	40.386	40.127	37.772	37.651
V_B (Å^3)	5.979	5.855	8.630	8.889	7.769	7.890
V_A/V_B	4.255	4.239	4.680	4.514	4.862	4.772
θ_x (°)	16.89	17.05	10.27	13.64	6.88	8.90
θ_y (°)	16.89	17.05	10.27	13.71	6.88	8.91
θ_z (°)	16.79	17.03	12.06	13.19	7.58	9.72
$\langle\phi_c\rangle$ (°)	12.19	12.24	5.79	10.05	4.32	5.90
$\langle\phi_a\rangle$ (°)	12.05	12.25	8.55	9.48	5.36	6.72
η_A	0.9534	0.9529	0.9898	0.9686	0.9943	0.9893
η_B	1.0910	1.0939	1.0457	1.0549	1.0177	1.0285
a_1 (Å)	3.2981	3.2750	3.7272	3.7845	3.5989	3.6193
a_2 (Å)	3.2981	3.2750	3.7272	3.7647	3.5989	3.6138
a_3 (Å)	3.2981	3.2750	3.7272	3.7437	3.5989	3.6194
θ_{23} (°)	90	90	90	90.61	90	89.85
θ_{31} (°)	90	90	90	89.46	90	89.75
θ_{12} (°)	90	90	90	89.69	90	89.71
λ_{PC}	0	0	0	0.0037	0	0.0007
σ_{PC}	0	0	0	0.012	0	0.004

general, experimental difficulties limit the pressure range over which full structure refinements can be obtained, a common practice being to report the variation of unit-cell parameters over a wider pressure range by means of the third-order Birch–Murnaghan equation of state [equation (7)].

$$P = \frac{3K_T}{2}\left[\left(\frac{V_0}{V}\right)^{7/3} - \left(\frac{V_0}{V}\right)^{5/3}\right]\left\{1 + \frac{3}{4}\left(K_0' - 4\right)\left[\left(\frac{V_0}{V}\right)^{2/3} - 1\right]\right\} \quad (7)$$

Here, coefficient K_T is the bulk modulus and K_0' is its derivative with respect to pressure. V_0 represents the reference unit-cell volume. The appropriate notation to use for the variation of cell parameters a, b, c with pressure would be K_{a0}, K_{a0}', a_0 *etc.*, whereby cubes a^3, b^3, c^3 will have been used for the Birch–Murnaghan fitting. It is also common to quote linear compressibilities β_a, β_b, β_c, whereby $\beta_a = (\partial/\partial P)(a/a_0)_T$, *etc.*, these generally holding over a limited pressure range. By setting K_0' values equal to 4, the term in curly brackets is equal to one, giving rise to the second-order Birch–Murnaghan equation.

The primary motivation for studying perovskites under pressure has been to simulate $MgSiO_3$ perovskite in the lower mantle, for which a phase transition to a post-perovskite phase at pressures > 125 GPa and a temperature of 2700 K has been proposed (Murakami *et al.*, 2004). This system is simulated by assuming regular octahedra in the following sub-section.

4.1. Simulation of $MgSiO_3$ under pressures of up to 125 GPa

It may be assumed that $MgSiO_3$ remains in space group *Pbnm* at all pressures up to ∼125 GPa. Accordingly, the 12 sets of a, b, c unit-cell parameters reported by Vanpeteghem *et al.* (2006) at pressures up to 10 GPa were used to derive the following Birch–Murnaghan constants to second order for the

Table 11
Structural parameters for $(La_{1-x}Nd_x)GaO_3$ in space groups *Pbnm* and $R\bar{3}c$.

x	Space group	p (GPa)	ICSD	η_A	η_B	$\langle\phi_c\rangle$ (°)	$\langle\phi_a\rangle$ (°)	$(\langle\phi_a\rangle + \langle\phi_c\rangle)/2$ (°)	V_A (Å^3)	V_A (Å^3)	V_A/V_B
0	*Pbnm*	0.0001	160233	0.9926 (2)	1.0406 (7)	4.90 (8)	8.5 (1)	6.69 (7)	48.653 (8)	10.299 (8)	4.724 (4)
	Pbnm	2.038 (10)	160235	0.9939 (2)	1.0382 (7)	4.46 (7)	8.3 (1)	6.39 (7)	48.136 (7)	10.146 (7)	4.744 (4)
	$R\bar{3}c$	2.356 (7)	160265	0.9868 (3)			6.56 (7)		48.024 (9)	10.066 (8)	4.771 (5)
	$R\bar{3}c$	8.127 (23)	160270	0.9872 (3)			6.45 (7)		46.745 (8)	9.782 (8)	4.779 (4)
0.06	*Pbnm*	0.0001	160236	0.9902 (4)	1.044 (2)	5.7 (1)	9.1 (3)	7.4 (1)	48.50 (2)	10.33 (2)	4.693 (9)
	Pbnm	5.30 (5)	160240	0.9947 (4)	1.042 (2)	4.2 (2)	9.1 (3)	6.6 (2)	47.18 (2)	9.98 (2)	4.73 (1)
0.12	*Pbnm*	0.0001	160241	0.9907 (4)	1.040 (1)	5.5 (1)	8.5 (2)	7.0 (1)	48.55 (1)	10.29 (1)	4.716 (7)
	Pbnm	6.437 (7)	160243	0.9939 (3)	1.039 (1)	4.4 (1)	8.5 (2)	6.5 (1)	46.96 (1)	9.91 (1)	4.741 (6)
	$R\bar{3}c$	8.020 (2)	160271	0.9875 (5)			6.4 (1)		46.65 (2)	9.75 (1)	4.783 (9)
	$R\bar{3}c$	9.496 (13)	160272	0.9872 (4)			6.46 (9)		46.37 (1)	9.71 (1)	4.778 (6)
0.20	*Pbnm*	0.0001	160244	0.9884 (4)	1.0425 (7)	6.2 (1)	8.7 (1)	7.45 (7)	48.404 (9)	10.323 (8)	4.689 (5)
	Pbnm	8.671 (7)	160248	0.9931 (3)	1.042 (1)	4.7 (1)	8.8 (2)	6.79 (9)	46.38 (1)	9.83 (1)	4.720 (6)
0.62	*Pbnm*	0.0001	160250	0.9807 (5)	1.049 (1)	7.9 (1)	9.1 (1)	8.52 (8)	47.72 (1)	10.35 (1)	4.611 (6)
	Pbnm	9.432	160256	0.9842 (7)	1.046 (1)	7.2 (2)	8.9 (2)	8.0 (1)	45.60 (1)	9.81 (1)	4.648 (7)
1.00	*Pbnm*	0.0001	160257	0.9749 (5)	1.0537 (9)	9.00 (9)	9.6 (1)	9.28 (8)	47.18 (1)	10.36 (1)	4.555 (6)
	Pbnm	8.292 (9)	160264	0.9762 (4)	1.0514 (8)	8.78 (7)	9.4 (1)	9.11 (7)	45.324 (9)	9.909 (9)	4.574 (5)

unit-cell volume and a and c unit-cell parameters: K_T = 252.90 GPa; V_0 = 162.52 Å^3; $K_{T,a}$ = 232.11 GPa; $V_{0,a}$ = 109.08 Å^3; $K_{T,c}$ = 240.78 GPa; $V_{0,c}$ = 328.33 Å^3.

The assumption was made that these constants could extended to 125 GPa, thereby yielding theoretical a, b and c unit-cell parameters over this whole range. This process was validated by comparing the values obtained ('Extrapolated B-M') with values quoted by Murakami *et al.* (2004) and Fiquet *et al.* (2000). Acceptable agreement is found in Table 9.

200 equally spaced pressures were taken within the range up to 125 GPa and a, b, c values calculated from the above Birch–Murnaghan constants. Values of x(O1), y(O1), x(O2), y(O2) and z(O2) were allowed to vary within the core *Excel* Solver functionality for space group *Pbnm* (Fig. 7), so as to generate regular octahedra. The resulting variation of parameters η_A and η_B with pressure is shown in Fig. 11(*a*).

Parameter η_A decreases from 0.9576 at 0 GPa to 0.9529 at 125 GPa, which indicates an increase in c^+ tilting. By comparison, η_B increases from 1.0649 at 0 GPa to 1.0939 at 125 GPa, indicating an increase in a^- tilting. The effect of pressure is to drive the structure ever further into the *Pbnm* phase field. It is likely that the imminent phase transition to post-perovskite at 125 GPa is triggered by the strong O···O repulsions that will be associated with this degree of octahedral tilting.

4.2. Simulation of $YAlO_3$ at pressures up to 52 GPa

Ross *et al.* (2004) elucidated the response of the perovskite compound $YAlO_3$ at pressures up to 8 GPa by providing eight structural refinements of a synthetic single crystal. A *decrease* in octahedral tilting with pressure was found, which was ascribed to the AlO_6 octahedral compressibility being greater than that of the YO_{12} site. It follows that an approach towards cubic symmetry will occur, similar to the *T*-series with *A* ion perturbation in §3.1. The Birch–Murnaghan constants to third order quoted by Ross *et al.* (2004) were used to generate unit-cell parameters at different pressures, as in §4.1. Two alternative simulations were carried out for pressures up to 8 GPa, the first assuming regular octahedra as in §4.1, and the second exploiting the octahedral distortions reported by Ross *et al.* (2004) from an analysis of their structural refinements. For this purpose, the linear, decreasing trends in the three different Al—O bond lengths with increasing pressure observed by them were translated into linear relationships for PCRO parameters a_1 to a_3. In addition, linear relationships for PCRO angle parameters θ_{23}, θ_{31} and θ_{12} were derived [equations (8)].

$$\begin{aligned} a_1\,(\text{Å}) &= 3.8421 - 0.007137\,[p(\text{GPa})] \\ a_2\,(\text{Å}) &= 3.8161 - 0.006407\,[p(\text{GPa})] \\ a_3\,(\text{Å}) &= 3.7915 - 0.005836\,[p(\text{GPa})] \\ \theta_{23}\,(^\circ) &= 90.893 - 0.034905\,[p(\text{GPa})] \\ \theta_{31}\,(^\circ) &= 89.382 + 0.010050\,[p(\text{GPa})] \\ \theta_{12}\,(^\circ) &= 89.878 - 0.019462\,[p(\text{GPa})] \end{aligned} \tag{8}$$

Solver-based refinements in *Pbnm* were carried out at equally spaced pressure values, the spacing determined by covering the pressure range from 0 to 60 GPa with 200 values. Parameters x(O1), y(O1), x(O2), y(O2) and z(O2) were allowed to vary in refinements with end-point determined by the minimum deviation from conditions (8). The deviation was observed to range between 0.001 and 0.050%.

The results of both simulations are shown in Fig. 11(*b*) and in that part of Fig. 11(*c*) with the blue-shaded background. The slope of both η_B curves is negative, compared to the positive slope of η_B for $MgSiO_3$. The slope of η_A for the simulation with regular octahedra is positive, compared to the negative slope for $MgSiO_3$. The opposite behaviour to $MgSiO_3$ is shown by $YAlO_3$, which shows a gradual progression away from *Pbnm* towards higher symmetry. The curve for η_A for distorted octahedra has a shallow minimum at ∼3.4 GPa, which is more clearly seen in Fig. 11(*c*). Thereafter η_A rises, as for undistorted octahedra.

[4] Values of K_T and V_0 are in good agreement with the values quoted by Vanpeteghem *et al.* (2006): 253 (1) GPa and 162.51 (2) Å^3.

Table 12
Structural parameters for eleven structural refinements of Ardit *et al.* (2017) on $YAl_{0.25}Cr_{0.75}O_3$.

p (GPa)	η_A	η_B	$\langle\phi_c\rangle$ (°) (§2.3)	$\langle\phi_a\rangle$ (°) (§2.3)	$\langle\phi_c\rangle$ (°) (Ardit)	$\langle\phi_a\rangle$ (°) (Ardit)	V_A (Å^3)	V_B (Å^3)	V_A/V_B
0.05 (5)	0.9557 (9)	1.082 (1)	11.9 (1)	11.7 (2)	12.0 (5)	16.6 (5)	43.52 (2)	10.10 (2)	4.309 (8)
1.44 (9)	0.9604 (4)	1.0868 (7)	11.24 (6)	12.32 (9)	12.7 (5)	16.6 (5)	43.238 (9)	10.030 (8)	4.311 (4)
3.32 (9)	0.9609 (5)	1.0862 (7)	11.18 (7)	12.32 (9)	12.7 (5)	16.5 (5)	42.892 (9)	9.938 (8)	4.316 (4)
4.93 (7)	0.9603 (5)	1.0871 (7)	11.25 (7)	12.36 (9)	12.8 (5)	16.6 (5)	42.561 (9)	9.878 (8)	4.309 (4)
6.36 (8)	0.9630 (5)	1.0890 (7)	10.88 (7)	12.67 (9)	13.1 (5)	16.5 (5)	42.321 (9)	9.812 (8)	4.313 (4)
8.48 (9)	0.9630 (5)	1.0890 (8)	10.88 (7)	12.67 (9)	13.1 (5)	16.6 (5)	41.954 (9)	9.727 (8)	4.313 (5)
10.54 (9)	0.9635 (6)	1.090 (1)	10.81 (9)	12.8 (1)	13.2 (5)	16.6 (5)	41.60 (1)	9.65 (1)	4.312 (6)
12.34 (7)	0.9580 (6)	1.086 (1)	11.57 (8)	12.2 (1)	12.6 (5)	16.5 (5)	41.28 (1)	9.59 (1)	4.303 (6)
14.40 (9)	0.9569 (8)	1.085 (1)	11.7 (1)	12.1 (2)	12.4 (5)	16.6 (5)	40.97 (1)	9.52 (1)	4.302 (7)
16.45 (9)	0.956 (1)	1.084 (2)	11.9 (2)	12.0 (2)	12.4 (5)	16.5 (5)	40.65 (2)	9.45 (2)	4.30 (1)
18.86 (9)	0.959 (2)	1.087 (3)	11.4 (3)	12.6 (3)	13.0 (5)	16.5 (5)	40.30 (3)	9.36 (3)	4.30 (2)

Table 13
Summary of innovations in the current work.

Innovation	Benefits
Quantification of distortion of centrosymmetric octahedra via PCRO.	(*a*) Direct, concise visualization of octahedral distortion. (*b*) Variation of PCRO parameters rooted in space group symmetry. (*c*) New possibilities for simulating perovskite structures at extrapolated (*p*–*T*–*X*) conditions. (*d*) Many more visualizable structural parameters *cf.* Thomas (1998). (*e*) Upgradable to non-centrosymmetric octahedra, and so applicable to all perovskites and more widely to all crystal structures containing octahedra. (*f*) Provides summary distortion parameters λ and σ.
Generalized algorithms for calculating tilt angles [ϕ_a, ϕ_b] and ϕ_c.	(*a*) Extension to space groups *Cmcm*, $P4_2/nmc$ and $R\bar{3}c$ not previously covered by analytical approximations. (*b*) Ability to calculate tilt angles in structures with distorted octahedra without approximation.
Structural parameters η_A and η_B.	(*a*) η_A emphasizes the importance of AX_8 inner polyhedra and focuses on octahedral tilting around the z (3) axis. (*b*) η_B focuses on tilting around the x (1) and y (2) axes. (*c*) Tracking structural evolution via η_A and η_B allows phase transitions between *Pbnm* and *Ibmm*, *Cmcm*, *I*4/*mcm* or *P*4/*mbm* to be rationalized and anticipated. (*d*) Improved integration with the tilt classification of Glazer (1972), and, by implication, group-theoretical methods.
Implementation in *Excel* Solver software environment.	(*a*) Reversibility of transformation between crystallographic and structural parameters. (*b*) The *Excel* file in the supporting information is a useful resource for calculating tilt angles and other parameters, as well as for refining crystallographic parameters under structural constraints. (*c*) Upgradable to other programming languages (Frontline Systems Inc., 2021).
Simulation of structural development at increasing pressure.	The assumption of regular or idealized distorted octahedra allows the prediction of crystal structure and associated parameters, *e.g.* η_A, η_B from unit-cell parameters alone. The potential for modelling structures and phase transitions at high pressure is thereby increased.

In a computational experiment, the pressure was allowed to rise towards 60 GPa, with unit-cell constants calculated from the Birch–Murnaghan constants of Ross *et al.* (2004) for the pressure range up to 8 GPa. Fig. 11(*c*) shows that the curvature of both pairs of curves changes sign as the octahedra change from regular to distorted. Since the constraints in equations (8) only apply up to 8 GPa, it became increasingly difficult to reach low deviations at the end-points of the refinements. The maximum deviation amounted to 1.08%, which was obtained at the highest pressure.

The ascending curve for η_A with distorted octahedra in Fig. 11(*c*) reaches zero at a pressure of ∼41.5 GPa. This would be consistent with a phase transition to *Ibmm* [*cf.* Figs. 10(*a*) and 10(*b*)]. By comparison, the η_B curve is the first to reach zero in the simulation with regular octahedra. The corresponding pressure is ∼51.6 GPa. This would be consistent with a phase transition to *I*4/*mcm* or *P*4/*mbm* [*cf.* Fig. 10(*d*)]. The asymptotic approach of the η_B curve to 1 for regular octahedra gives rise to a broad pressure range in which *Cmcm* could be stabilized as well as *Pbnm* prior to this phase transition. This phenomenon has been observed in $NaTaO_3$ by Knight & Kennedy (2015) over a broad *temperature* range, as discussed in §3.1.4. Assuming pattern similarity, a phase change to *P*4/*mbm* would be anticipated at 51.6 GPa. More generally, the simulations of $YAlO_3$, both with and without octahedral distortion, indicate how this distortion is expected to have a direct effect on the sequence of phase transitions and the pressures at which they occur.

In summary, the analysis of (*p*–*T*–*X*)-induced phase transitions in terms of η_A and η_B parameters is a stimulus to further, targeted experimental work on the systems that have been analysed and simulated in §3.1, §4.1 and §4.2.

4.3. Crystal structures generated in the high-pressure simulations

A by-product of the simulations in §3.1 is the generation of full sets of oxygen ion coordinates. Table 10 contains these data corresponding to the conditions denoted by dashed lines in Figs. 11(*a*) and 11(*c*). The space group is *Pbmn* with the B ions in 4*b* positions. The full set of associated structural parameters is also quoted below the line in the table.

In all cases, the effect of increasing pressure is to reduce V_A and V_B. However, the ratio V_A/V_B is reduced in $MgSiO_3$ and increased in $YAlO_3$. This signifies movement further into the *Pbnm* phase field in the former case [Fig. 11(*a*)] and movement away towards higher symmetry in the latter [Fig. 11(*c*)]. This is borne out by the changes in inclination angles θ_x, θ_x, θ_x, tilt angles ϕ_a, ϕ_c and tilt-related parameters η_A, η_B.

4.4. Analysis of $(La_{1-x}Nd_x)GaO_3$ structures at pressures of up to 12 GPa

Apart from the above simulations, the structural parameters used in this work are applied to the structural refinements of Angel *et al.* (2007) for this 3:3 perovskite solid solution. In carrying out *A*-ion substitutional perturbations, it was found that a phase transition from *Pbnm* to $R\bar{3}c$ takes place under pressure for x values up to 0.20, but not for $x = 0.62$ or $x = 1$. The question arises as to whether a particular pattern of structural evolution within the *Pbnm* phase is associated with a phase transition to $R\bar{3}c$. Data for the *Pbmn* and $R\bar{3}c$ phases at their lowest and highest investigated pressures for a given x value are given in Table 11.

The direct influence of the *A*-ion perturbations is seen in the values of V_A, which decrease downwards in the table with increasing x for the $p = 0.0001$ GPa values. Since V_B remains approximately constant, a parallel trend of decreasing V_A/V_B ratio with increasing x is generally observed. This is consistent with greater stabilization within the *Pbnm* phase field. Pressure induces the opposite trend to raising x, since the V_A/V_B ratios for maximum pressures within the *Pbnm* phase field are uniformly higher than at atmospheric pressure. A parallel increase in η_A and decrease in η_B is observed. At lower x values up to 0.20, which are associated with reduced *Pbnm* stabilization, the increased pressure induces a phase transition to $R\bar{3}c$. Angel *et al.* (2007) report the following approximate pressures for this phase transition: $x = 0$: 2.2 GPa; $x = 0.06$: 5.5 GPa; $x = 0.12$: 7.8 GPa; $x = 0.20$: 12 GPa. The expected cross-correlations between parameter pairs $\eta_A \leftrightarrow \phi_c$ and $\eta_B \leftrightarrow \phi_a$ are observed within the *Pbnm* phase field: the greater the magnitude of the deviations of η_A and η_B from one, the larger the $\langle\phi_c\rangle$ and $\langle\phi_a\rangle$ angles. It is proposed that the observed fall in $\langle\phi_c\rangle$ to $\sim$4.2–4.4° with increasing pressure is the principal driving force for the phase transitions to $R\bar{3}c$. After the transitions for $x = 0$ and $x = 0.12$, *i.e.* within the $R\bar{3}c$ phase field, the ϕ_a tilt angle is larger and approximately equal to the mean tilt angle $(\langle\phi_a\rangle + \langle\phi_c\rangle)/2$ in the *Pbnm* field beforehand. For $x = 0.62$ and $x = 1.00$, the critical range of ϕ_c between 4.2 and 4.4° is not reached at the pressures investigated, so that these compounds remain stabilized in space group *Pbnm*.

4.5. Structural parameters for $YAl_{0.25}Cr_{0.75}O_3$ with locked octahedral tilting

Ardit *et al.* (2017) subsequently took up the theme of locked octahedral tilting in orthorhombic 3:3 perovskites (*A* ion +3; *B* ion +3) by reference to the solid solution $YAl_{0.25}Cr_{0.75}O_3$ in space group *Pbnm*. Although in general agreement with Zhao *et al.* (2004) and Angel *et al.* (2005) in assuming compressibility ratios $\beta(AO_{12})/\beta(BO_6) < 1$ for a 3:3 perovskite and > 1 for a 2:4 perovskite, their compound showed a compressibility ratio approximately equal to one (Table 12).

In spite of consistently falling V_A and V_B values with increasing pressure, the V_A/V_B ratio remains approximately constant, as do parameters η_A, η_B, $\langle\phi_c\rangle$ and $\langle\phi_a\rangle$. Discrepancies are observed between the values of the tilt angles calculated according to §2.3 and the values quoted by Ardit *et al.* (2017) without declaring the method of calculation. This is not unexpected, as discussed in §2.4. Since values of $\langle\phi_c\rangle$ and $\langle\phi_a\rangle$ calculated according to §2.3 show the expected cross-correlations between parameter pairs $\eta_A \leftrightarrow \phi_c$ and $\eta_B \leftrightarrow \phi_a$, indirect support is given for the correctness of these calculations.

5. Discussion

The ability of the method to analyse experimental structural data and the sequences of phase transitions between space groups has been demonstrated in §3 and §4. By comparison with the group-theoretical approach, it has not been necessary to relate these explicitly to the cubic aristotype, since deviations of V_A/V_B from the limiting value of 5 in the aristotype provide a direct indication of how far away a given structure is from the aristotype. Parameters V_A, V_B and V_A/V_B continue to yield valuable insight, for example in Table 11. However, the direct calculation of Glazer tilt angles ϕ_c and $[\phi_a, \phi_b]$ and associated derived parameters η_A and η_B has allowed a deeper analysis of the structural factors leading to phase transitions than a consideration of these volumes alone. The significance of the generalized algorithms introduced here for the Glazer tilt angles may be assessed by reference to Wang & Angel (2011): '...the decomposition of a perovskite structure including tilted and distorted octahedra by geometric analysis does not result in an unambiguous definition of the Glazer (1972) tilts and the problem is more acute in perovskites with lower space-group symmetries'. These authors noted further that 'unambiguous expressions for both the Glazer tilts and their relationship to the V_A/V_B ratio are still to be determined explicitly for each space group, and in a general form'. These observations led Wang & Angel (2011) to resort to group-theoretical methods in order to relate the amplitudes of symmetry-adapted modes to V_A/V_B ratio. The current work, by comparison, has remained strictly based on unit-cell parameters and atomic coordinates. Although it has not provided generalized analytical expressions for these tilt angles, it has led to two generalized algorithms (*a*) for all centrosymmetric space groups apart from $R\bar{3}c$ and (*b*) for space group $R\bar{3}c$ (and more generally, triclinic space groups). An analytical link between ϕ_c, $[\phi_a, \phi_b]$ and V_A/V_B has not

been provided, since inclination angles θ_1 to θ_3 are more suitable for this purpose [equation (1)]. However, the linked-cell implementation within *Excel* allows the empirical derivation of numerical relationships between Glazer tilt angles and V_A/V_B.

The methodological innovations of the current work and their benefits are summarized in Table 13.

The question of the relative stability of alternative perovskite phases has been addressed by several workers employing quantum-mechanical methods (Zagorac *et al.*, 2014) as well as the semi-empirical bond-valence method. Woodward (1997*b*) initiated this discussion by evaluating the ionic and covalent bonding in perovskites and analysing the conditions of stabilization of favoured tilt systems $a^-a^-c^+$, $a^-a^-a^-$ and $a^0a^0a^0$. In later work (Lufaso & Woodward, 2001), an algorithm was developed to minimize the so-called global instability index (GII) in alternative tilt systems, this being the r.m.s. deviation between calculated bond valences and ideal cationic valences. The bond-valence method was also the favoured approach of Zhao *et al.* (2004) in rationalizing the relative compressibilities of the AO_{12} and BO_6 polyhedra in perovskites. It led to a clear differentiation in behaviour between 2:4 and 3:3 perovskites, which has remained a feature of experimentally led investigations of perovskites under pressure, for example by Ardit *et al.* (2017).

The potential of direct transformation of crystallographic data into structural parameters for the analysis of sequences of phase transitions has been demonstrated in this work. The set of structural parameters has been extended and a baseline provided for future investigations of non-centrosymmetric perovskites. The intention is to promote more detailed interaction between experimental crystallography and modelling in developing new materials by atomic and molecular design.

6. Related literature

The following references are cited in the supporting information: Hahn (1995), Williams (1971).

Acknowledgements

I thank student Yannick Breuer and an unknown referee of the article by Fricke & Thomas (2021) for rekindling my interest in perovskites. Thanks are likewise due to an anonymous referee of this article for some good suggestions. Finally, the work of staff of the Rheinische Landesbibliothek in Koblenz in retrieving numerous scientific articles is gratefully acknowledged. Open access funding enabled and organized by Projekt DEAL.

References

Ahtee, M. & Darlington, C. N. W. (1980). *Acta Cryst.* B**36**, 1007–1014.
Ali, R. & Yashima, M. (2005). *J. Solid State Chem.* **178**, 2867–2872.
Angel, R. J., Zhao, J. & Ross, N. L. (2005). *Phys. Rev. Lett.* **95**, 025503-1.
Angel, R. J., Zhao, J., Ross, N. L., Jakeways, C. V., Redfern, S. A. T. & Berkowski, M. (2007). *J. Solid State Chem.* **180**, 3408–3424.
Ardit, M., Dondi, M. & Cruciani, G. (2017). *Phys. Rev. B*, **95**, 024110-1.
Arulnesan, S. W., Kayser, P., Kennedy, B. J. & Knight, K. S. (2016). *J. Solid State Chem.* **238**, 109–112.
Darlington, C. N. W. & Knight, K. S. (1999). *Acta Cryst.* B**55**, 24–30.
Fiquet, G., Dewaele, A., Andrault, D., Kunz, M. & Le Bihan, T. (2000). *Geophys. Res. Lett.* **27**, 21–24.
Fricke, M. & Thomas, N. W. (2021). *Acta Cryst.* B**77**, 427–440.
Frontline Systems Inc. (2021). https://www.solver.com/.
Fu, W. T. & Ijdo, D. J. W. (1995). *Solid State Commun.* **95**, 581–585.
Fu, W. T., Visser, D. & IJdo, D. J. W. (2005). *Solid State Commun.* **134**, 647–652.
Fu, W. T., Visser, D., Knight, K. S. & IJdo, D. J. W. (2007). *J. Solid State Chem.* **180**, 1559–1565.
Glazer, A. M. (1972). *Acta Cryst.* B**28**, 3384–3392.
Glazer, A. M. (1975). *Acta Cryst.* A**31**, 756–762.
Hahn, T. (1995). Editor. *International Tables for Crystallography*, Vol. A, *Space-Group Symmetry*. Dordrecht: Kluwer.
Howard, C. J. & Stokes, H. T. (1998). *Acta Cryst.* B**54**, 782–789.
Howard, C. J. & Stokes, H. T. (2002). *Acta Cryst.* B**58**, 565–565.
Ivanov, S. A., Eriksson, S.-G., Tellgren, R. & Rundlöf, H. (2001). *Mater. Sci. Forum*, **378–381**, 511–516.
Jena, A. K., Kulkarni, A. & Miyasaka, T. (2019). *Chem. Rev.* **119**, 3036–3103.
Kennedy, B. J., Howard, C. J. & Chakoumakos, B. C. (1999). *J. Phys. Condens. Matter*, **11**, 1479–1488.
Kennedy, B. J., Howard, C. J., Thorogood, G. J. & Hester, J. R. (2001). *J. Solid State Chem.* **161**, 106–112.
Kennedy, B. J., Hunter, B. A. & Hester, J. R. (2002). *Phys. Rev. B*, **65**, 224103-1.
Kennedy, B. J., Prodjosantoso, A. K. & Howard, C. J. (1999). *J. Phys. Condens. Matter*, **11**, 6319–6327.
Kennedy, B. J., Yamaura, K. & Takayama-Muromachi, E. (2004). *J. Phys. Chem. Solids*, **65**, 1065–1069.
Knight, K. S. (2009). *Can. Mineral.* **47**, 381–400.
Knight, K. S. & Kennedy, B. J. (2015). *Solid State Sci.* **43**, 15–21.
Li, L., Kennedy, B. J., Kubota, Y., Kato, K. & Garrett, R. F. (2004). *J. Mater. Chem.* **14**, 263–273.
Liu, X. & Liebermann, R. C. (1993). *Phys. Chem. Miner.* **20**, 171–175.
Lufaso, M. W. & Woodward, P. M. (2001). *Acta Cryst.* B**57**, 725–738.
Magyari-Köpe, B., Vitos, L., Johansson, B. & Kollár, J. (2001). *Acta Cryst.* B**57**, 491–496.
Magyari-Köpe, B., Vitos, L., Johansson, B. & Kollár, J. (2002). *Phys. Rev. B*, **66**, 092103–1.
Megaw, H. D. (1973). *Crystal Structures – A Working Approach*, pp. 285–302. London: Saunders.
Mitchell, R. H. (2002*a*). *Perovskites: Modern and Ancient*, Preface. Thunder Bay, Ontario: Almaz Press.
Mitchell, R. H. (2002*b*). *Perovskites: Modern and Ancient*, pp. 27–29. Thunder Bay, Ontario: Almaz Press.
Mitchell, R. H., Burns, P. C., Knight, K. S., Howard, C. J. & Chakhmouradian, A. R. (2014). *Phys. Chem. Miner.* **41**, 393–401.
Mitchell, R. H. & Liferovich, R. P. (2004). *J. Solid State Chem.* **177**, 4420–4427.
Mountstevens, E. H., Attfield, J. P. & Redfern, S. A. T. (2003). *J. Phys. Condens. Matter*, **15**, 8315–8326.
Moussa, S. M., Kennedy, B. J. & Vogt, T. (2001). *Solid State Commun.* **119**, 549–552.
Murakami, M., Hirose, K., Kawamura, K., Sata, N. & Ohishi, Y. (2004). *Science*, **304**, 855–858.
Redfern, S. A. T. (1996). *J. Phys. Condens. Matter*, **8**, 8267–8275.
Reifenberg, M. & Thomas, N. W. (2018). *Acta Cryst.* B**74**, 165–181.
Ross, N. L., Zhao, J. & Angel, R. J. (2004). *J. Solid State Chem.* **177**, 1276–1284.
Sasaki, S., Prewitt, C. T., Bass, J. D. & Schulze, W. A. (1987). *Acta Cryst.* C**43**, 1668–1674.
Shannon, R. D. (1976). *Acta Cryst.* A**32**, 751–767.
Shrout, T. R. & Zhang, S. J. (2007). *J. Electroceram.* **19**, 113–126.

Tamazyan, R. & van Smaalen, S. (2007). *Acta Cryst.* B**63**, 190–200.
Thomas, N. W. (1989). *Acta Cryst.* B**45**, 337–344.
Thomas, N. W. (1996). *Acta Cryst.* B**52**, 16–31.
Thomas, N. W. (1998). *Acta Cryst.* B**54**, 585–599.
Thomas, N. W. (2017). *Acta Cryst.* B**73**, 74–86.
Vanpeteghem, C. B., Zhao, J., Angel, R. J., Ross, N. L. & Bolfan-Casanova, N. (2006). *Geophys. Res. Lett.* **33**, L03306-1.
Wang, D. & Angel, R. J. (2011). *Acta Cryst.* B**67**, 302–314.
Williams, D. E. (1971). *Acta Cryst.* A**27**, 452–455.
Woodward, P. M. (1997*a*). *Acta Cryst.* B**53**, 32–43.
Woodward, P. M. (1997*b*). *Acta Cryst.* B**53**, 44–66.
Yang, J. (2008). *Acta Cryst.* B**64**, 281–286.
Yashima, M. & Ali, R. (2009). *Solid State Ionics*, **180**, 120–126.
Zagorac, J., Zagorac, D., Zarubica, A., Schön, J. C., Djuris, K. & Matovic, B. (2014). *Acta Cryst.* B**70**, 809–819.
Zhao, J., Ross, N. L. & Angel, R. J. (2004). *Acta Cryst.* B**60**, 263–271.